nature COMMUNICATIONS

ARTICLE

DOI: 10.1038/s41467-018-04015-z OPEN

Inducing skyrmions in ultrathin Fe films by hydrogen exposure

Pin-Jui Hsu[1,2], Levente Rózsa[1,3], Aurore Finco[1], Lorenz Schmidt[1], Krisztián Palotás[4,5], Elena Vedmedenko[1], László Udvardi[6,7], László Szunyogh[6,7], André Kubetzka[1], Kirsten von Bergmann[1] & Roland Wiesendanger[1]

Magnetic skyrmions are localized nanometer-sized spin configurations with particle-like properties, which are envisioned to be used as bits in next-generation information technology. An essential step toward future skyrmion-based applications is to engineer key magnetic parameters for developing and stabilizing individual magnetic skyrmions. Here we demonstrate the tuning of the non-collinear magnetic state of an Fe double layer on an Ir(111) substrate by loading the sample with atomic hydrogen. By using spin-polarized scanning tunneling microscopy, we discover that the hydrogenated system supports the formation of skyrmions in external magnetic fields, while the pristine Fe double layer does not. Based on ab initio calculations, we attribute this effect to the tuning of the Heisenberg exchange and the Dzyaloshinsky–Moriya interactions due to hydrogenation. In addition to interface engineering, hydrogenation of thin magnetic films offers a unique pathway to design and optimize the skyrmionic states in low-dimensional magnetic materials.

[1] Department of Physics, University of Hamburg, 20355 Hamburg, Germany. [2] Department of Physics, National Tsing Hua University, 30013 Hsinchu, Taiwan. [3] Institute for Solid State Physics and Optics, Wigner Research Centre for Physics, Hungarian Academy of Sciences, Budapest 1525, Hungary. [4] Institute of Physics, Slovak Academy of Sciences, 84511 Bratislava, Slovakia. [5] MTA-SZTE Reaction Kinetics and Surface Chemistry Research Group, University of Szeged, Szeged 6720, Hungary. [6] Department of Theoretical Physics, Budapest University of Technology and Economics, Budapest 1111, Hungary. [7] MTA-BME Condensed Matter Research Group, Budapest University of Technology and Economics, Budapest 1111, Hungary. Correspondence and requests for materials should be addressed to P.-J.H. (email: pinjuihsu@phys.nthu.edu.tw) or to L.Róz. (email: rozsa.levente@physnet.uni-hamburg.de)

Magnetic skyrmions are whirling spin textures displaying topological properties[1–4]. They offer promising perspectives for the future development of information technology based on their nanoscale size[5], robustness against defects[6], motion driven by low current densities[7], and the skyrmion Hall effect[8]. In order to engineer key features of the particle-like magnetic skyrmions, it is essential to tune the magnetic parameters of the thin films as well as their interfaces. In the presence of strong spin–orbit coupling, the Dzyaloshinsky–Moriya interaction[9,10] (DMI) emerges at surfaces and interfaces, which favors the formation of non-collinear spin states such as skyrmions. The magnetic ground state of the film is usually determined by the balance of the DMI energy, the magnetocrystalline anisotropy energy, the Zeeman energy, and the symmetric Heisenberg exchange interaction energy. The Heisenberg exchange can also contribute to the formation of skyrmions if ferromagnetic nearest-neighbor and antiferromagnetic next-nearest-neighbor interactions are taken into account[11].

In the quest for a knowledge-based material design for future skyrmionic devices, different routes are pursued. Up to date, the most widespread method for tuning magnetic parameters is interface engineering based on the growth of multilayered heterostructures. For example, by adding a Pd overlayer on top of Fe/Ir(111), the emergence of individual nanoscale magnetic skyrmions could be demonstrated by low-temperature spin-polarized scanning tunneling microscopy[5,12] (SP-STM). Moreover, sandwiching Co layers between different types of heavy metals led to the observation of magnetic skyrmions at room temperature[13–15], which has been explained by an enhancement of the DMI due to the multiple interfaces involved.

The role of hydrogen in the material embrittlement in metals and alloys stimulated detailed investigations on its molecular kinetics of adsorption, dissociation, and diffusion on and below metal surfaces[16,17]. The incorporation of hydrogen can significantly influence the magnetic properties of materials[18], for example by changing the effective magnetic moment, modifying the magnetic anisotropy[19–21], or tuning the interlayer exchange coupling[22]. However, very little is known about the role of hydrogen in tailoring non-collinear spin states, in particular, inducing magnetic skyrmions in ultrathin films and multilayers by means of hydrogen exposure has not been reported yet.

In the present study, we first demonstrate the tuning of the magnetic properties of the zero-field ground state in an Fe double layer on an Ir(111) single crystal substrate by loading the sample with atomic hydrogen. We observe two structural phases with distinct magnetic states. One of these hydrogen-induced phases (H1-Fe) is characterized by a spin spiral ground state with an increased magnetic period, by about a factor of three, compared to the spin spiral state of the pristine Fe double layer[23] (Fe-DL). The other hydrogen-induced phase (H2-Fe) is found to be ferromagnetic. With applied magnetic field, a transition from the hydrogen-induced spin spiral state to a magnetic skyrmion state is demonstrated experimentally and reproduced by simulations based on Heisenberg exchange interaction and DMI parameters determined from ab initio calculations. Remarkably, such a transition does not occur for the pristine Fe-DL, at least up to a magnetic field of 9 T. This drastic effect of hydrogen on non-collinear spin structures opens a further avenue for tuning the microscopic magnetic interactions responsible for creating and stabilizing individual skyrmions in ultrathin films as required for the future development of skyrmion-based devices.

Results

Hydrogen-induced structural phases. Our earlier SP-STM studies of ultrathin Fe films on Ir(111) have demonstrated that the Fe monolayer (Fe-ML) grows pseudomorphically and exhibits a nanoskyrmion lattice with a magnetic period of about one nanometer[24]. When more Fe is deposited onto the Ir substrate, the tensile strain increases and the Fe-DL locally relieves the strain by the incorporation of dislocation lines[23]. Figure 1a shows a constant-current STM topography image of a sample with about 1.6 atomic layers of Fe on Ir(111), where pseudomorphic ($Fe\text{-}DL_{ps}$) and reconstructed ($Fe\text{-}DL_{rc}$) double-layer Fe areas coexist. The magnetic ground state of the pseudomorphic Fe-DL is a spin spiral state with a period of about 1.2 nm, which is stable in external magnetic fields of up to 9 T[23]. The morphology of the Fe-DL changes upon hydrogen exposure and subsequent annealing: as seen in Fig. 1b, the number of dislocation lines in the Fe-DL is significantly decreased and two different commensurate superstructures emerge, see high-resolution image in Fig. 1c. On the right side of Fig. 1c, a hexagonal lattice with twice the lattice constant of the substrate is observed, i.e., a $p(2 \times 2)$ superstructure with respect to the Ir(111) surface, which we assign to a hydrogen-loaded Fe-DL. Note that the modulation on the several nm scale in Fig. 1c is due to the magnetic structure of the film and will be discussed together with Fig. 2. On

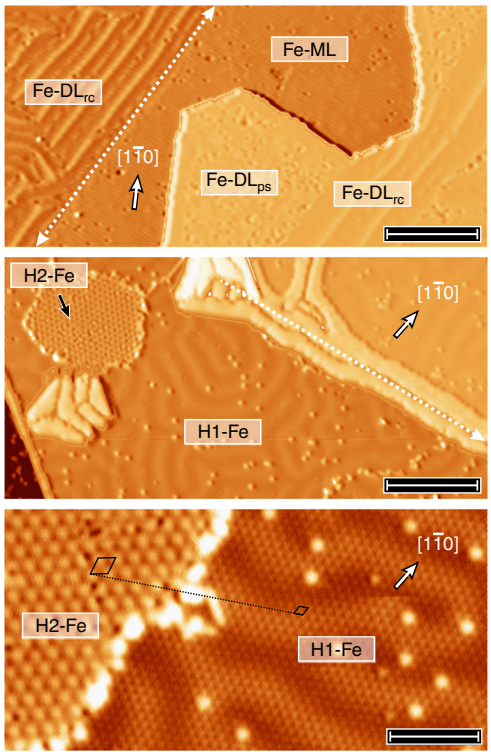

Fig. 1 The pristine and the hydrogenated Fe double layer on Ir(111). **a** STM constant-current topography image of a sample with about 1.6 atomic layers of Fe grown on Ir(111). The dashed white line indicates a buried Ir step. The Fe-ML grows pseudomorphically, while the Fe-DL pseudomorphic areas (ps) coexist with a reconstruction (rc) formed by dislocation lines along the $[11\bar{2}]$ direction. Scale bar 15 nm. **b** STM constant-current topography image after hydrogen exposure (4.8 L) of a sample of about 2.3 atomic layers of Fe on Ir(111). The dashed white line indicates a buried Ir step. Two different H-induced superstructures on the Fe-DL are visible. Scale bar 15 nm. **c** Magnified view of the two hydrogen-induced superstructures on the Fe-DL. While the H1-Fe phase forms a $p(2 \times 2)$ superstructure, the H2-Fe phase has a larger unit cell and is rotated with respect to the high-symmetry directions. Scale bar 5 nm. Measurement parameters: $U = +0.2$ V for **a** and $U = -0.2$ V for **b**, **c**. $I = 1$ nA; $T = 4$–5 K; $B = 0$ T; W tip in **a** and Cr bulk tip in **b**, **c**. The images are partially differentiated and the contrast levels have been adjusted separately for different terraces

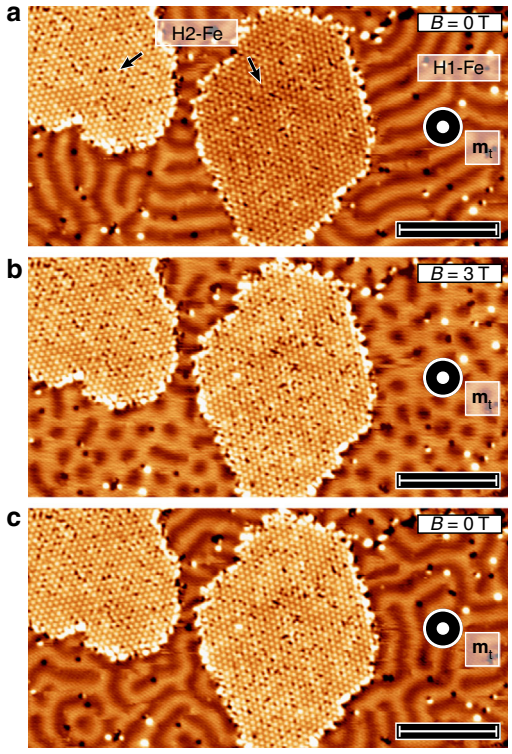

Fig. 2 SP-STM images of the two different H-Fe double-layer areas at different applied magnetic fields. **a** SP-STM constant-current image of the H-induced superstructures on the Fe-DL without external magnetic field B. The apex of the Cr bulk tip has its magnetic moment $\mathbf{m_t}$ perpendicular to the surface, thus the tip is sensitive to the out-of-plane magnetization components of the sample. The periodic modulation of the contrasts for H1-Fe demonstrates spin spiral order, whereas the two-level contrast on H2-Fe reflects its ferromagnetic ground state. **b** Same as **a** but in a perpendicular magnetic field of $B = 3$ T. The dark dots and the surrounding brighter area in H1-Fe are magnetized in opposite out-of-plane directions. Both islands of H2-Fe now show the same magnetic contrast, i.e., they are magnetized along the same direction. **c** Same as **a**, also in zero-magnetic field. In this remanent state, the spin spiral in the H1-Fe area is more disordered and the H2-Fe islands remain in their field-polarized states. Measurement parameters: $U = -0.7$ V; $I = 1$ nA; $T = 4.2$ K. Scale bars 15 nm

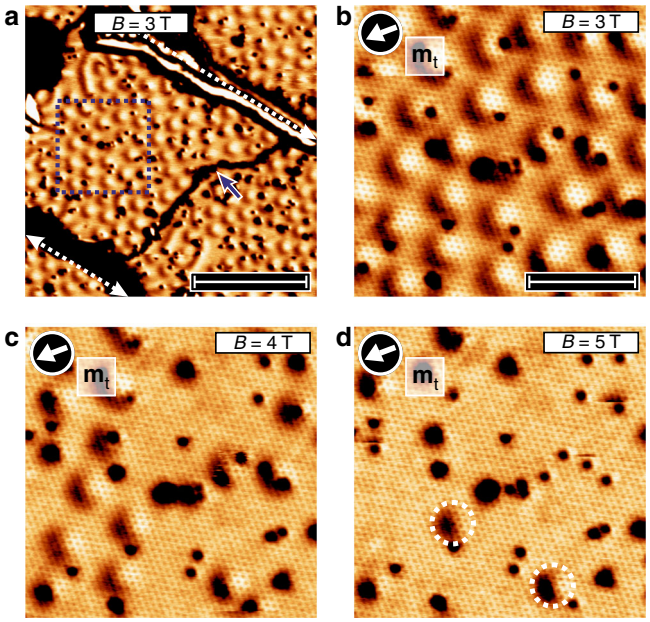

Fig. 3 Magnetic skyrmions in the H1-Fe phase. **a** SP-STM map of differential tunneling conductance of the hydrogenated Fe-DL, with large H1-Fe areas on three adjacent terraces. The Cr bulk tip used for this measurement is sensitive to the in-plane components of the sample magnetization; the dashed white lines are buried Ir steps and the black line indicated by the blue arrow is a phase domain between adjacent H1-Fe areas on the same terrace. It is evident that all magnetic objects show the identical spin-dependent two-lobe contrast, which demonstrates that they are skyrmions with unique rotational sense. Scale bar 25 nm. **b**–**d** Magnified views of the magnetic skyrmions at increasing external magnetic fields as indicated in the panels. Scale bar 8 nm. In **d**, two remaining skyrmions are shown by circles. For corresponding STM topography images, see Supplementary Fig. 4. Measurement parameters: $U = -0.2$ V; $I = 1$ nA; $T = 4.2$ K

the left side of Fig. 1c, a slightly rotated hexagonal superstructure with a larger lattice constant of 0.98 nm is observed, which is caused by a different hydrogen-induced phase of the Fe-DL. In the following, we refer to these two hydrogen-induced phases of the Fe-DL as H1-Fe and H2-Fe—see Supplementary Note 1 and Supplementary Figs. 1–3 for more details including atomic defects and possible structural models. Whereas these two phases might simply arise from different hydrogen concentrations, their sharp transition regions and a much higher stability of H2-Fe against tip-induced changes indicate different vertical positions of the hydrogen atoms with respect to the surface.

Stabilization of individual magnetic skyrmions. To investigate the magnetic state of the hydrogenated Fe-DL phases, we performed SP-STM measurements, which are sensitive to the projection of the local sample magnetization onto the quantization axis defined by the spin orientation of the probe tip[25]. Consequently, the measured spin-polarized tunnel current depends on the relative alignment of tip and sample magnetization, and the magnetic texture is reflected in constant-current SP-STM images such as the one in Fig. 2a. In the H1-Fe area, a modulation of magnetic origin can be observed with a period of about 3.5 nm due to the presence of a spin spiral state, but the $p(2 \times 2)$ atomic superstructure is not resolved at this scale. Two separate areas of the H2-Fe can be seen in Fig. 2a. They exhibit a relative height difference of about 6 pm. Upon application of an external magnetic field, see Fig. 2b, the two H2-Fe areas exhibit the same height. We conclude that the H2-Fe is ferromagnetic and that the two areas in Fig. 2a have opposite magnetization directions. Due to the application of a magnetic field (Fig. 2b), the magnetization of the right H2-Fe island is switched. In this external magnetic field of 3 T, the spin spiral phase of the H1-Fe with a period of 3.5 nm is transformed into dots, which here represent the out-of-plane magnetization component opposite to the applied magnetic field. When the magnetic field is removed (Fig. 1c), the magnetization direction of the H2-Fe areas remains unchanged, whereas the magnetic dots of the H1-Fe structure transform back into a spin spiral phase, which differs only in details compared to the previous zero-magnetic-field state in Fig. 2a.

For examining the spin texture of the H1-Fe in more detail, we used a spin-polarized tip that is sensitive to the in-plane components of the sample magnetization. The magnetic objects emerging at 3 T with a diameter of about 3 nm are now imaged as two-lobe structures, and the brighter signal is always on the same side, see Fig. 3a and the magnified view in Fig. 3b. This is a signature of magnetic skyrmions with unique rotational sense[5]. When the external magnetic field is increased, see Fig. 3b–d, the field-polarized state is favored and the number of magnetic skyrmions decreases. In addition, due to the associated Zeeman energy, also the size of the individual magnetic skyrmions shrinks. Note that the features that remain unchanged by the

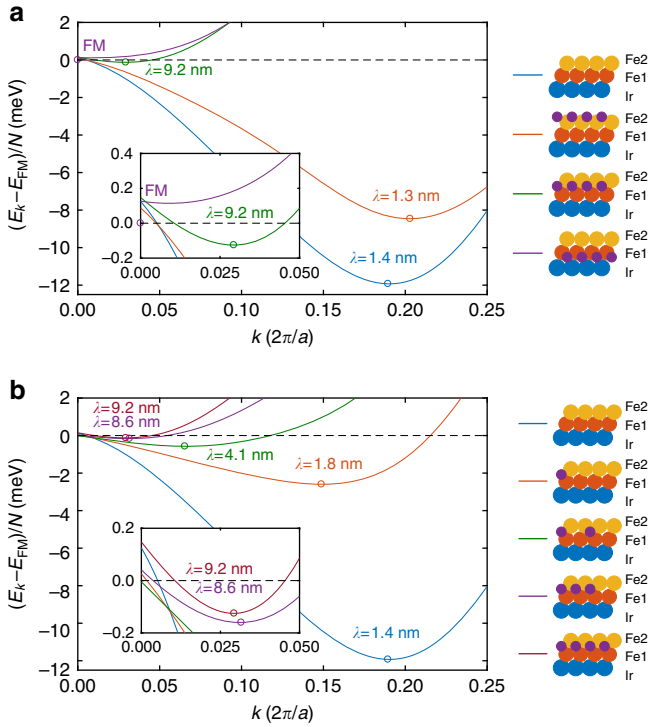

Fig. 4 Influence of the H adsorption site and H concentration on the magnetic ground state from ab initio calculations. Energies of harmonic cycloidal spin spiral states per spin as a function of wave vector along the $[11\bar{2}]$ direction compared to the ferromagnetic state. **a** Dependence on adsorption site. From top to bottom in the legend: Fe double layer, H above the Fe layers in fcc hollow sites, H between the Fe layers in octahedral sites, and H between Ir and Fe in octahedral sites. **b** Dependence on H concentration. The concentration increases in steps of 0.25 ML from top to bottom in the legend. Circles denote the location of the minima converted to the magnetic period length $\lambda = 2\pi/k$, with the lattice constant a = 2.71 Å. The energy of the spiral at zero wave vector differs from that of the ferromagnetic state due to the magnetic anisotropy energy

external magnetic field are due to defects, see also Supplementary Note 2 and Supplementary Fig. 4.

Ab initio calculations. To understand the role of hydrogen for the different magnetic states in the Fe-DL, density-functional theory calculations were performed. Both the position and the concentration of H atoms were varied, for more details, see the Methods section, Supplementary Notes 3 and 4 and Supplementary Tables 1–4. The results for H layers in different vertical positions with respect to the surface are summarized in Fig. 4a, displaying the energy of the magnetic system as a function of spin spiral wave vector k. The ferromagnetic state is located at $k = 0$, and as k is increased the angle between neighboring spins in the lattice also increases. For the pristine Fe-DL, which continues the fcc stacking of the Ir(111), we obtain a spin spiral ground state with a period of 1.4 nm (Fig. 4a), close to the experimentally observed value of 1.2 nm for pseudomorphic growth. In agreement with previous results for ultrathin Fe films on the Ir(111) surface[12,24], we find a right-handed cycloidal rotation of the spin spirals originating from interfacial DMI. When a full layer of H is adsorbed above the Fe layers in fcc hollow sites, the magnetic period of the spin spiral ground state decreases slightly to 1.3 nm, i.e., in this configuration, the H does not considerably alter the magnetic ground state. In comparison, a significant increase of the magnetic period to 9.2 nm is observed for a layer of H adsorbed in octahedral sites between the Fe atomic layers. Finally, the calculations show that the ground state is ferromagnetic when the H is placed in octahedral sites at the Fe–Ir interface.

These drastic differences in the magnetic ordering may be attributed to the strong dependence of the microscopic magnetic interactions on the hybridization between the atoms, including direct hopping processes between the Fe atoms and indirect processes mediated by the Ir substrate or the H atoms. As demonstrated in Fig. 4, the hybridization sensitively depends on the vertical and horizontal adsorption site of hydrogen. However, since the overlap of the wave functions is directly connected to the distance between the atoms, we find a strong correlation between the interlayer distances and the period of the obtained magnetic ground state. It has been demonstrated in earlier publications[12,24,26–28] that the strong hybridization between the Ir and Fe atoms is responsible for the formation of non-collinear ground states with short magnetic periods in similar systems, and that a decreased interlayer distance leads to a reduction in the period length. If the H is adsorbed between the two Fe layers, it increases their distance by about 30 pm compared to the pristine Fe-DL, while the adsorption at the Fe–Ir interface increases both the Ir–Fe1 and Fe1–Fe2 distances by about 20 pm. In comparison, if the H is adsorbed above the Fe layers, it only has a minimal effect on the interlayer distances (cf. refs. [18,29]) and the magnetic structure. For more details on the interlayer distances, see Supplementary Note 3 and Supplementary Tables 1–3.

Based on these results, we can explain the experimentally observed ferromagnetic H2-Fe phase by the incorporation of H at the Fe–Ir interface in octahedral sites, see calculated ferromagnetic ground state in Fig. 4a. In contrast, the H1-Fe phase exhibits a spin spiral ground state with a period of ~3.5 nm. Comparison with the calculations suggests that this phase might be due to H atoms being located between the two Fe layers, but with an intermediate H concentration between the H-free Fe-DL with a spin spiral period of 1.4 nm and the complete H layer with 9.2 nm, see Fig. 4a. This assignment is in agreement with the experimental indications that the hydrogen in the two different H-Fe phases is located in different vertical positions with respect to the surface.

In the theoretical calculations, we increased the concentration of H atoms between the Fe layers in steps of 0.25 ML, and indeed found a gradual enhancement of the magnetic period from 1.4 to 9.2 nm as displayed in Fig. 4b. At the same time, the distance between the Fe layers increases, meaning that the outer Fe2 layer becomes less hybridized with the inner Fe1 layer and the Ir substrate as discussed above. Our calculations reveal that in this geometry the hybridization between the Fe and H orbitals also contributes to the increase of the magnetic period independently of the layer separation—for a more detailed discussion, see Supplementary Note 5 and Supplementary Fig. 5.

Spin model calculations. Our results show that both a change of the vertical position of H atoms as well as a variation of the H concentration can lead to modified magnetic properties of the hydrogenated Fe-DL. In the following, we look in more detail into those two systems, which represent best the experimentally observed H1-Fe and H2-Fe phases, i.e. the one with 0.50 ML of H between the Fe layers and the one where the H is located at the Fe–Ir interface, corresponding to the spin spiral ground state with 4.1 nm period in Fig. 4b and the FM ground state in Fig. 4a. To obtain a deeper understanding of the microscopic mechanisms, we derive effective interaction parameters based on the spin spiral dispersion relations (Fig. 4), described by the Hamiltonian

$$H = -\tfrac{1}{2}\sum_{<i,j>_1} J_1 \mathbf{S}_i\mathbf{S}_j - \tfrac{1}{2}\sum_{<i,j>_2} J_2 \mathbf{S}_i\mathbf{S}_j - \tfrac{1}{2}\sum_{<i,j>_1} \mathbf{D}_{ij}\left(\mathbf{S}_i \times \mathbf{S}_j\right) - \sum_i K\left(S_i^z\right)^2 - \sum_i \mu_s B S_i^z. \quad (1)$$

Table 1 Parameters used for the spin dynamics simulations

System	Fe-DL	H1-Fe	H2-Fe
J_1 (meV)	33.18	51.00	65.14
J_2 (meV)	−17.14	−17.00	−19.72
D (meV)	−1.36	−1.09	−0.27
K (meV)	0.25	−0.01	0.25
μ_s (μ_B)	2.89	2.84	2.58
$f=(J_1+3J_2)/J_1$	−0.55	0.00	0.09

Spin model parameters used for describing the low-energy behavior of the magnetic systems considered in the ab initio calculations—see Eq. (1). The Fe-DL, H1-Fe, and H2-Fe parameter sets describe the ab initio calculations for the pristine Fe-DL (top curve in the legend of Fig. 4a), 0.50 ML H in octahedral positions between the Fe layers (middle curve in the legend of Fig. 4b) and H in octahedral positions between Ir and Fe (bottom curve in the legend of Fig. 4a), respectively. Negative values of $f=(J_1+3J_2)/J_1$ mean that the Heisenberg exchange interactions prefer a non-collinear ground state. Positive and negative values for the atomic Heisenberg exchange interactions denote ferromagnetic and antiferromagnetic couplings, respectively. The negative sign of the DMI indicates a right-handed rotation of the spin spiral. For the anisotropy, positive and negative values describe easy-axis and easy-plane types, respectively

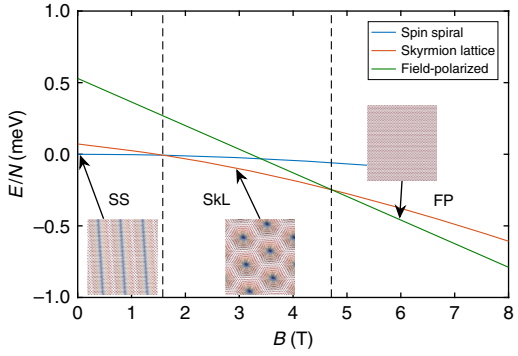

Fig. 5 Results of the spin dynamics simulations. Zero-temperature phase diagram of the model describing the H1-Fe system with the parameters from Table 1, displaying the energy per spin in different magnetic structures as a function of the strength of the external field B applied perpendicular to the surface. Dashed black lines indicate the transition fields between the spin spiral, skyrmion lattice, and field-polarized states. Insets display the ground states observed at selected field values

The system is modeled by classical spins $\mathbf{S}_i$ occupying atomic positions of a single-layer hexagonal lattice, with nearest- and next-nearest-neighbor Heisenberg exchange interactions J_1, J_2, nearest-neighbor DMI $|\mathbf{D}_{ij}|=D$, on-site anisotropy K, atomic magnetic moment μ_s, and the external field B applied perpendicularly to the surface. Analogously to a micromagnetic description, the model given by Eq. (1) is expected to correctly describe the system's properties only at long wavelengths and low energies—see Supplementary Note 6 and Supplementary Figs. 6 and 7 for more details.

The derived parameters are summarized in Table 1 for the Fe-DL, the H1-Fe, and H2-Fe structures. Within the description of Eq. (1), two mechanisms may prefer a non-collinear order of the spins, namely the DMI and the frustration of the symmetric Heisenberg exchange interactions[11], the latter of which is encapsulated in the dimensionless parameter $f=(J_1+3J_2)/J_1$, where negative values indicate a spin spiral ground state—see Supplementary Note 6 and Supplementary Table 5 for details. For the pristine Fe-DL, the calculations yield $f<0$, meaning that frustration plays an indispensable role in the formation of the spin spiral ground state; the rather large DMI of −1.36 meV (or −6.99 mJ m^{-2}) also favors non-collinear magnetic order and leads to a right-handed unique rotational sense. In contrast, in the H1-Fe, the frustration of symmetric Heisenberg exchange interactions is reduced ($f\approx 0$) due to the increase of J_1; here, the non-collinear magnetic ground state can form only because of the significant value of the DMI (−1.09 meV or −6.05 mJ m^{-2}). The ferromagnetic ground state for the H2-Fe arises because $f>0$, and at the same time, the DMI is nearly quenched (−0.27 meV or −1.46 mJ m^{-2}) and cannot compete with the collinearity enforced by the large J_1 and the out-of-plane anisotropy. We attribute this pronounced decrease in the DMI to the significant increase of the Fe–Ir interlayer distance in the H2-Fe phase, which presumably reduces the hopping processes between the magnetic layer and the substrate exhibiting high spin–orbit coupling, regarded as the main mechanism for the emergence of interfacial DMI[10,30]. Finally, Fig. 5 displays the low-temperature phase diagram of the H1-Fe structure obtained from spin dynamics simulations, with illustrations of the resulting spin spiral, skyrmion lattice, and field-polarized ground states. The skyrmion lattice phase is the ground state in a regime from about 1.6 to 4.8 T, in good agreement with the magnetic field regime where magnetic skyrmions are observed experimentally (Fig. 3). For the pristine Fe-DL, the simulations agree with the experiments in determining a spin spiral ground state up to field values of 9 T.

Discussion

As shown in Fig. 2, both the H1-Fe and the H2-Fe structures display two kinds of point defects appearing as bright protrusions and dark pits in the STM constant-current topography images. According to a series of growth studies in Supplementary Note 1 and Supplementary Figs. 1 and 2, repeated dosages of hydrogen on the sample lead to a decrease in the number of bright protrusions and an increase in the number of dark pits, which makes it possible to identify the former as hydrogen vacancies and the latter as additional hydrogen atoms. Note that the defects can have a reversed contrast in differential tunneling conductance images as shown in Fig. 3 and described in detail in Supplementary Note 2 and Supplementary Fig. 4.

As demonstrated in ref. [31] for the Pd/Fe/Ir(111) system, surface defects act as local perturbations on the potential landscape, exhibiting pinning effects on non-collinear magnetic spin textures. Figures 1–3 display that in the H1-Fe structure, both types of defects tend to prefer in-plane magnetization directions, being primarily located off the centers of skyrmions (Fig. 3) or at the boundary between the up and down magnetized areas of spin spirals as imaged by an out-of-plane magnetized tip (Fig. 2a, c). Vacancies and additional adatoms may also be thought of as local modifications of the hydrogen concentration between or above the Fe layers, which change the magnetic interactions between the Fe atoms—see also Supplementary Note 5 and Supplementary Fig. 5.

However, our measurements indicate that the atomic-scale defects only have a minor influence on the nanometer-scale spin spiral period and the size of magnetic skyrmions. Furthermore, we always found that the pristine Fe-DL is in the spin spiral state and the H2-Fe structure is in the ferromagnetic state, regardless of the presence of dislocation lines, defects, or the value of the external magnetic field up to 9 T. Magnetic skyrmions can only be stabilized in the H1-Fe structure, and although the field value necessary for collapsing them into the field-polarized state slightly depends on the local defects[31], skyrmions can typically be observed between 3 and 5 T. This means that at a fixed external field value, the hydrogen-induced magnetic state is stable, and can only be structurally transformed into a disordered phase, for example, by an intentional increase of hydrogen dosage or extreme tunneling conditions as discussed in Supplementary Note 1 and Supplementary Fig. 2. We expect that the preparation of a well-defined and extended H1-Fe phase becomes possible after optimizing the amount of hydrogen and the annealing temperature as illustrated by the growth studies in Supplementary Note 1 and Supplementary Fig. 1.

In conclusion, we demonstrated how the magnetic parameters and the corresponding magnetic period length in ultrathin Fe films may be tuned by hydrogen exposure. SP-STM measurements performed on an Fe-DL on Ir(111) revealed two hydrogenated phases with different atomic structures. While the H2-Fe structure is ferromagnetic, the H1-Fe structure displays a spin spiral ground state at zero field and skyrmions with a unique rotational sense in the presence of an applied field. Ab initio calculations suggest that the incorporation of H into different vertical positions and in different concentrations leads to a modification of the frustrated Heisenberg exchange interactions and DMI responsible for the formation of non-collinear magnetic order. This can result either in a ferromagnetic ground state or in an increase of the spin spiral period and the appearance of skyrmions in applied magnetic fields.

Most recent propositions for tailoring the magnetic interactions for skyrmion applications have focused on the appropriate choice of the magnetic layer or the heavy metal materials with strong spin–orbit coupling responsible for the appearance of interfacial DMI[12,15,32]. As demonstrated in this paper, the adsorption of non-magnetic elements with low atomic numbers such as hydrogen can also result in a significant modulation of the interactions directly by hybridization with the magnetic atoms and indirectly by modifying the atomic structure, which influences the hybridization between the magnetic layer and the substrate. This phenomenon, which is expected to be ubiquitous for impurities of low-Z elements[33], can potentially be turned into a new platform for the controlled design and development of skyrmionic materials.

Methods

Sample preparation and characterization. A clean surface of the Ir(111) substrate was prepared in ultra-high vacuum with a base pressure of $\leqq 1 \times 10^{-10}$ mbar. Cycles of Ar^+ ion sputtering with an emission current of 25 mA and a beam energy of 800 eV were performed at an Ar gas pressure of about 8×10^{-5} mbar. A sample current of about 10 μA was detected during the Ar^+ ion sputtering. Besides that, several cycles of oxygen annealing of Ir(111) was carried out by varying the substrate temperature from room temperature to 1350 °C under oxygen exposure. The oxygen pressure was reduced stepwise from 5×10^{-6} mbar to 5×10^{-8} mbar.

After the Ir(111) substrate was clean, about 1.5–2.5 ML of Fe was evaporated with a deposition rate of about 0.5 ML per min using molecular beam epitaxy. These films were subsequently exposed to atomic hydrogen obtained by cracking hydrogen gas molecules at high temperature in a dedicated hydrogen source. An amount of 4.8 L of atomic hydrogen was dosed onto the Fe-DL/Ir(111) at room temperature, followed by a post-annealing treatment at about 600 K for 10 min, resulting in extended areas of hydrogenated Fe. The effect of the amount of hydrogen and the post-annealing treatment is discussed in more detail in Supplementary Note 1 and Supplementary Figs. 1 and 2.

SP-STM measurements. SP-STM measurements were performed by using chemically etched bulk Cr tips in a home-built low-temperature STM setup cooled down to 4.2 K by liquid helium. For topographic images, the STM was operated in the constant-current mode with the bias voltage (U) applied to the sample. Differential tunneling conductance (dI/dU) maps were acquired by lock-in technique with a small voltage modulation U_{mod} (10–30 mV) added to the bias voltage and a modulation frequency of 5–6 kHz. External magnetic fields of up to 9 T were applied to the sample along the out-of-plane direction.

For bulk Cr tips, the magnetization direction of the tip apex atom determines the quantization axis of the spin sensitivity. Because this direction is not known a priori, we derive it from the measured images and symmetry considerations. The reconstructed Fe-DL displays three rotational domains of spin spirals with 120° angle between the wave vector directions in the different domains[23]. Both in-plane and out-of-plane magnetized tips are sensitive to the spiral modulation. However, while all rotational domains of spin spirals have the same corrugation amplitude with an out-of-plane sensitive tip, they are imaged with different amplitudes when the tip is sensitive to in-plane components[23]. For example, when the in-plane tip magnetization is parallel to the propagation direction of a cycloidal spin spiral, one observes maximum magnetic contrast, whereas the amplitude in the other two rotational domains is reduced by a factor of cos(±120°). Magnetic skyrmions imaged with a spin-polarized tip sensitive to the out-of-plane component appear axially symmetric. When an in-plane sensitive tip is used, the magnetic contribution to the signal vanishes for the center of the skyrmion and its surrounding, because there tip and sample magnetizations are orthogonal. Instead the maximum magnetic contrast is observed on the in-plane parts of the skyrmion that are parallel or antiparallel to the tip magnetization, and a two-lobe structure appears. When the two-lobe structures of all skyrmions appear the same, they have the same rotational sense due to the interfacial DMI[5,34]. Magnetic skyrmions stabilized by interfacial DMI are typically cycloidal due to the symmetry selection rules[6,35,36].

Density-functional theory calculations. Geometry optimizations were carried out using the Vienna Ab initio Simulation Package[37–39] (VASP). The Fe double layer was modeled by 7 Ir and 2 Fe atomic layers in fcc growth within a 1×1 unit cell, with about 18 Å empty space vertically between the slabs. We used $a = 2.71$ Å for the in-plane lattice constant of the Ir(111) surface. Different H adsorption sites were investigated by adding a H layer to the above slab. Varying the H concentration was performed by using a 2×2 unit cell and 1, 2 or 3 H atoms between the Fe layers, corresponding to 0.25, 0.50 and 0.75 ML coverages, respectively. We used pseudopotentials from the projector-augmented wave method with the Perdew–Wang 91 (PW91) parametrization[40] of the generalized gradient approximation, and a $15 \times 15 \times 1$ Monkhorst–Pack $\mathbf{k}$-mesh. The vertical positions of the top Ir, the two Fe and the H layers were allowed to relax until the forces became smaller than 0.01 eV $Å^{-1}$. We determined the Bader charges belonging to the atoms by using the method from refs. [41–43].

The magnetic structure was studied by using the fully relativistic Screened Korringa–Kohn–Rostoker (SKKR) method[44,45] within the atomic sphere approximation. For the pristine Fe-DL, we used 10 Ir and 2 Fe layers, as well as 3 layers of empty spheres (vacuum) between semi-infinite bulk Ir and semi-infinite vacuum in a 1×1 unit cell. For the hydrogenated system, we used 9 Ir, 2 Fe, 1 H, and 3 vacuum layers. The interlayer distances corresponded to the values optimized by VASP, and the radii of the atomic spheres were determined in a way that minimizes overlap, with the Bader charges computed from VASP serving as a benchmark against which the charges within the atomic spheres were compared. Partial H coverages were considered by applying the coherent potential approximation in a 1×1 unit cell, corresponding to a random occupation of the available adsorption sites with the probability determined by the H concentration. The vertical positions corresponded to the averaged value over atoms belonging to the same layer from VASP. For the self-consistent calculations, the Vosko–Wilk–Nusair parametrization[46] for the exchange–correlation potential was used within the local spin density approximation. We applied the relativistic torque method[47] to determine the magnetocrystalline anisotropy energy, as well as pairwise Heisenberg exchanges and DMIs between the Fe atoms within a radius of $8a$, corresponding to 240 intralayer and 225 interlayer neighbors for each spin. From the spin model parameters, we calculated the energy per spin in a harmonic cycloidal spin spiral configuration,

$$\mathbf{S}_i = \mathbf{n}\cos\mathbf{k}\mathbf{R}_i \pm \hat{\mathbf{k}}\sin\mathbf{k}\mathbf{R}_i, \quad (2)$$

where $\mathbf{n}$ is the outwards pointing normal vector of the surface, $\mathbf{k}$ is the in-plane wave vector with direction $\hat{\mathbf{k}}$, and the ± signs describe right- and left-handed rotational senses, respectively. The simplified model parameters displayed in Table 1 were obtained by calculating the spin spiral dispersion relation from Eq. (1) and fitting it to the dispersion relation determined based on ab initio calculations at the center of the Brillouin zone encompassing the minimum position. The self-consistent calculations also yielded the spin magnetic moments, the value of which was averaged over the two Fe layers to obtain μ_s.

Spin dynamics simulations. The field dependence of the magnetic ground state was studied on a 128×128 hexagonal lattice with periodic boundary conditions using the simplified model parameters discussed above. For the H1-Fe system, three different spin configurations were considered: a cycloidal spin spiral state with wave vector minimizing the energy in the absence of external field, a skyrmion lattice corresponding to a triple-$\mathbf{k}$ state constructed from the above wave vector, and the collinear field-polarized state. The energy was minimized at each magnetic field value by the numerical solution of the stochastic Landau–Lifshitz–Gilbert equation[48]. The choice of Gilbert damping coefficient $\alpha = 1$ ensured fast convergence, and the energy differences between the final states of the simulations and the corresponding local energy minima were $\sim 10^{-6}$ meV per atom. The boundary conditions did not allow for a change in the wave vector during the simulations. The wave vector of the minimum energy state only weakly depends on the magnetic field, apart from a short range close to the transition between the skyrmion lattice and the field-polarized states.

Data availability. The data supporting the findings of this study are available from the corresponding authors upon request.

Received: 8 November 2017 Accepted: 27 March 2018
Published online: 20 April 2018

References

1. Bogdanov, A. N. & Yablonskii, D. A. Thermodynamically stable vortices in magnetically ordered crystals. The mixed state of magnets. *Sov. Phys. JETP* **68**, 101–103 (1989).
2. Rößler, U. K., Bogdanov, A. N. & Pfleiderer, C. Spontaneous skyrmion ground states in magnetic metals. *Nature* **442**, 797–801 (2006).
3. Yu, X. Z. et al. Real-space observation of a two-dimensional skyrmion crystal. *Nature* **465**, 901–904 (2010).

4. Nayak, A. K. et al. Magnetic antiskyrmions above room temperature in tetragonal Heusler materials. *Nature* **548**, 561–566 (2017).
5. Romming, N. et al. Writing and deleting single magnetic skyrmions. *Science* **341**, 636–639 (2013).
6. Fert, A., Cros, V. & Sampaio, J. Skyrmions on the track. *Nat. Nanotechnol.* **8**, 152–156 (2013).
7. Sampaio, J., Cros, V., Rohart, S., Thiaville, A. & Fert, A. Nucleation, stability and current-induced motion of isolated magnetic skyrmions in nanostructures. *Nat. Nanotechnol.* **8**, 839–844 (2013).
8. Jiang, W. et al. Direct observation of the skyrmion Hall effect. *Nat. Phys.* **13**, 162–169 (2017).
9. Dzyaloshinsky, I. A thermodynamic theory of weak ferromagnetism of antiferromagnetics. *J. Phys. Chem. Solids* **4**, 241–255 (1958).
10. Moriya, T. New mechanism of anisotropic superexchange interaction. *Phys. Rev. Lett.* **4**, 228–230 (1960).
11. Okubo, T., Chung, S. & Kawamura, H. Multiple-q states and the skyrmion lattice of the triangular-lattice Heisenberg antiferromagnet under magnetic fields. *Phys. Rev. Lett.* **108**, 017206 (2012).
12. Dupé, B., Hoffmann, M., Paillard, C. & Heinze, S. Tailoring magnetic skyrmions in ultra-thin transition metal films. *Nat. Commun.* **5**, 4030 (2014).
13. Jiang, W. et al. Blowing magnetic skyrmion bubbles. *Science* **349**, 283–286 (2015).
14. Moreau-Luchaire, C. et al. Additive interfacial chiral interaction in multilayers for stabilization of small individual skyrmions at room temperature. *Nat. Nanotechnol.* **11**, 444–448 (2016).
15. Soumyanarayanan, A. et al. Tunable room-temperature magnetic skyrmions in Ir/Fe/Co/Pt multilayers. *Nat. Mater.* **16**, 898–904 (2017).
16. Jiang, D. E. & Carter, E. A. Diffusion of interstitial hydrogen into and through bcc Fe from first principles. *Phys. Rev. B* **70**, 064102 (2004).
17. Arman, M. A. et al. Adsorption of hydrogen on stable and metastable Ir(100) surfaces. *Surf. Sci.* **656**, 66–76 (2017).
18. Máca, F., Kudrnovský, J., Drchal, V. & Redinger, J. Influence of oxygen and hydrogen adsorption on the magnetic structure of an ultrathin iron film on an Ir(001) surface. *Phys. Rev. B* **88**, 045423 (2013).
19. Dubout, Q. et al. Controlling the spin of Co atoms on Pt(111) by hydrogen adsorption. *Phys. Rev. Lett.* **114**, 106807 (2015).
20. Khajetoorians, A. A. et al. Tuning emergent magnetism in a Hund's impurity. *Nat. Nanotechnol.* **10**, 958–964 (2015).
21. Santos, B. et al. Hydrogen-induced reversible spin-reorientation transition and magnetic stripe domain phase in bilayer Co on Ru(0001). *Phys. Rev. B* **85**, 134409 (2012).
22. Hjörvarsson, B. et al. Reversible tuning of the magnetic exchange coupling in Fe/V(001) superlattices using hydrogen. *Phys. Rev. Lett.* **79**, 901–904 (1997).
23. Hsu, P.-J. et al. Guiding spin spirals by local uniaxial strain relief. *Phys. Rev. Lett.* **116**, 017201 (2016).
24. Heinze, S. et al. Spontaneous atomic-scale magnetic skyrmion lattice in two dimensions. *Nat. Phys.* **7**, 713–718 (2011).
25. Wiesendanger, R. Spin mapping at the nanoscale and atomic scale. *Rev. Mod. Phys.* **81**, 1495–1550 (2009).
26. Kudrnovský, J., Máca, F., Turek, I. & Redinger, J. Substrate-induced antiferromagnetism of a Fe monolayer on the Ir(001) surface. *Phys. Rev. B* **80**, 064405 (2009).
27. von Bergmann, K. et al. Observation of a complex nanoscale magnetic structure in a hexagonal Fe monolayer. *Phys. Rev. Lett.* **96**, 167203 (2006).
28. Simon, E., Palotás, K., Rózsa, L., Udvardi, L. & Szunyogh, L. Formation of magnetic skyrmions with tunable properties in PdFe bilayer deposited on Ir (111). *Phys. Rev. B* **90**, 094410 (2014).
29. Gallego, S., Sanchez, N., Martin, S., Muñoz, M. C. & Szunyogh, L. Reversible enhancement of the magnetism of ultrathin Co films by H adsorption. *Phys. Rev. B* **82**, 085414 (2010).
30. Fert, A. & Levy, P. M. Role of anisotropic exchange interactions in determining the properties of spin-glasses. *Phys. Rev. Lett.* **44**, 1538–1541 (1980).
31. Hanneken, C., Kubetzka, A., von Bergmann, K. & Wiesendanger, R. Pinning and movement of individual nanoscale magnetic skyrmions via defects. *New J. Phys.* **18**, 055009 (2016).
32. Dupé, B., Bihlmayer, G., Böttcher, M., Blügel, S. & Heinze, S. Engineering skyrmions in transition-metal multilayers for spintronics. *Nat. Commun.* **7**, 11779 (2016).
33. Belabbes, A., Bihlmayer, G., Blügel, S. & Manchon, A. Oxygen-enabled control of Dzyaloshinskii-Moriya interaction in ultra-thin magnetic films. *Sci. Rep.* **6**, 24634 (2016).
34. Romming, N., Kubetzka, A., Hanneken, C., von Bergmann, K. & Wiesendanger, R. Field-dependent size and shape of single magnetic skyrmions. *Phys. Rev. Lett.* **114**, 177203 (2015).
35. Moriya, T. Anisotropic superexchange interaction and weak ferromagnetism. *Phys. Rev.* **120**, 91–98 (1960).
36. von Bergmann, K., Kubetzka, A., Pietzsch, O. & Wiesendanger, R. Interface-induced chiral domain walls, spin spirals and skyrmions revealed by spin-polarized scanning tunneling microscopy. *J. Phys. Condens. Matter* **26**, 394002 (2014).
37. Kresse, G. & Furthmüller, J. Efficiency of ab-initio total energy calculations for metals and semiconductors using a plane-wave basis set. *Comput. Mater. Sci.* **6**, 15–50 (1996).
38. Kresse, G. & Furthmüller, J. Efficient iterative schemes for ab initio total-energy calculations using a plane-wave basis set. *Phys. Rev. B* **54**, 11169–11186 (1996).
39. Hafner, J. Ab-initio simulations of materials using VASP: density-functional theory and beyond. *J. Comput. Chem.* **29**, 2044–2078 (2008).
40. Perdew, J. P. & Wang, Y. Accurate and simple analytic representation of the electron-gas correlation energy. *Phys. Rev. B* **45**, 13244–13249 (1992).
41. Henkelman, G., Arnaldsson, A. & Jónsson, H. A fast and robust algorithm for Bader decomposition of charge density. *Comput. Mater. Sci.* **36**, 354–360 (2006).
42. Sanville, E., Kenny, S. D., Smith, R. & Henkelman, G. An improved grid-based algorithm for Bader charge allocation. *J. Comp. Chem.* **28**, 899–908 (2007).
43. Tang, W., Sanville, E. & Henkelman, G. A grid-based Bader analysis algorithm without lattice bias. *J. Phys. Condens. Matter* **21**, 084204 (2009).
44. Szunyogh, L., Újfalussy, B., Weinberger, P. & Kollár, J. Self-consistent localized KKR scheme for surfaces and interfaces. *Phys. Rev. B* **49**, 2721–2729 (1994).
45. Zeller, R., Dederichs, P. H., Újfalussy, B., Szunyogh, L. & Weinberger, P. Theory and convergence properties of the screened Korringa–Kohn–Rostoker method. *Phys. Rev. B* **52**, 8807–8812 (1995).
46. Vosko, S. H., Wilk, L. & Nusair, M. Accurate spin-dependent electron liquid correlation energies for local spin density calculations: a critical analysis. *Can. J. Phys.* **58**, 1200–1211 (1980).
47. Udvardi, L., Szunyogh, L., Palotás, K. & Weinberger, P. First-principles relativistic study of spin waves in thin magnetic films. *Phys. Rev. B* **68**, 104436 (2003).
48. Nowak, U. in *Handbook of Magnetism and Advanced Magnetic Materials* Vol. 2 (eds Kronmüller, H. & Parkin, S.) (Wiley, 2007).

Acknowledgements

We thank J. Hagemeister, N. Romming, M. Dupé, B. Dupé, and S. Heinze for insightful discussions. Financial support was provided by the Deutsche Forschungsgemeinschaft via SFB 668, by the European Union via the Horizon 2020 research and innovation program under grant agreement no. 665095 (MAGicSky), by the Alexander von Humboldt Foundation, by the National Research, Development and Innovation Office of Hungary under project nos. K115575 and FK124100, by the Slovak Academy of Sciences via the SASPRO Fellowship (project no. 1239/02/01), by the Tempus Foundation via the Hungarian State Eötvös Fellowship and by the MOST under project no. 107-2112-M007-001-MY3, Taiwan.

Author contributions

P.-J.H. performed the experiments. P.-J.H., A.F., L.S., A.K., and K.v.B. analyzed the data. L.R. and K.P. performed the VASP calculations. L.R., K.P., L.U., and L.S. performed the SKKR calculations and analyzed the results. L.R. and E.V. performed the spin dynamics simulations and discussed the data. P.-J.H. and L.R. prepared the figures, P.-J.H., K.v.B., L.R., and R.W. wrote the manuscript. All authors discussed the results and provided inputs to the manuscript.

Additional information

Supplementary Information accompanies this paper at https://doi.org/10.1038/s41467-018-04015-z.

Competing interests: The authors declare no competing interests.

Supplementary Information

Hsu, P.-J. et al. Inducing skyrmions in ultrathin Fe films by hydrogen exposure.

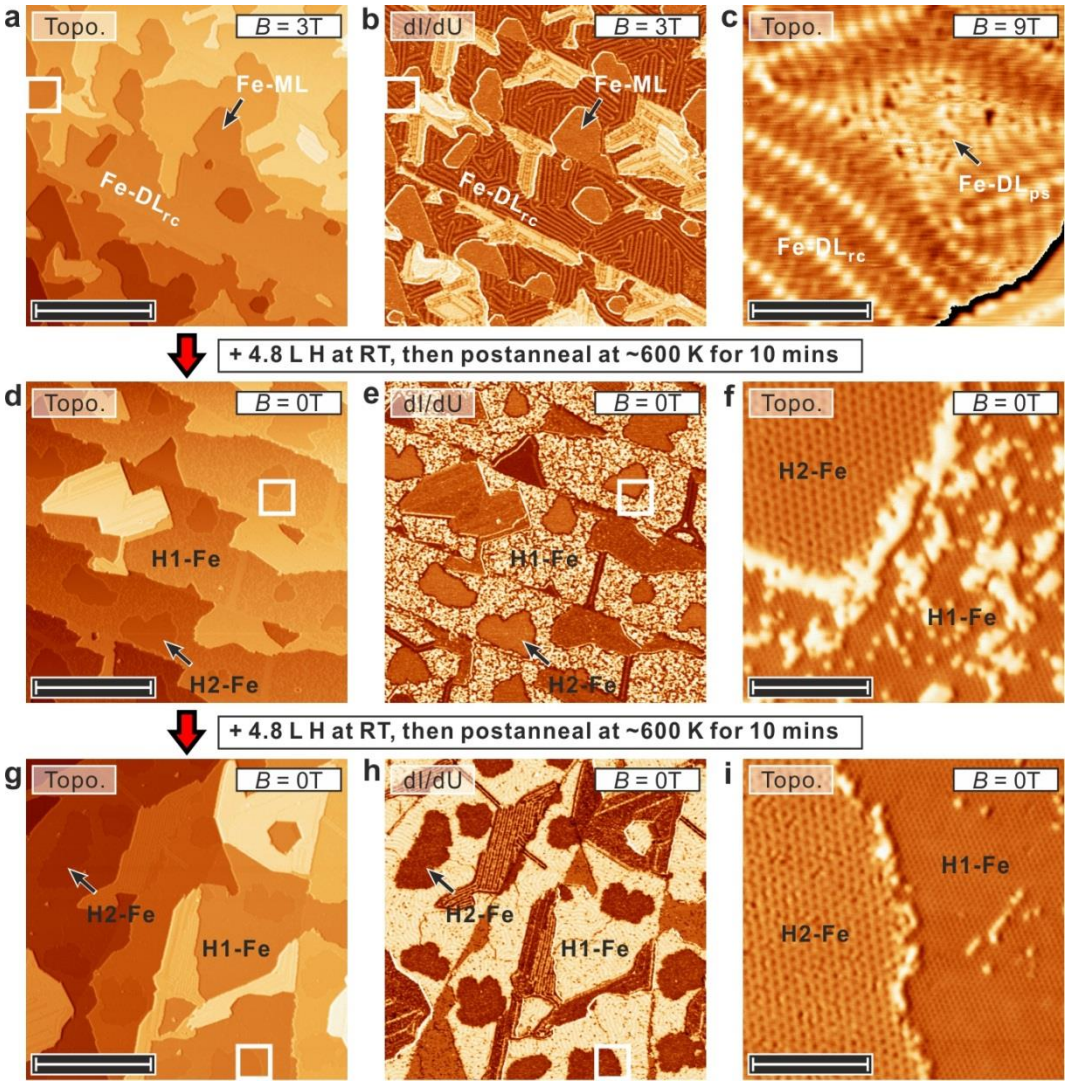

Supplementary Figure 1 | Hydrogenation of the Fe double layer on Ir(111). a,**-c**, SP-STM constant-current image, d*I*/d*U* map, and magnified view of about 2.2 atomic layers of Fe on Ir(111). The Fe was deposited with the Ir substrate held at about 500 K. **d**,**-f**, Same as in panels **a**-**c** after exposure of the same sample to 4.8 L of atomic hydrogen (4 min at pressure of $2 \cdot 10^{-8}$ mbar) at room temperature (the sample was removed from the 4.2 K STM about 1 h before exposure). After the hydrogen exposure the sample was annealed at about 600 K for 10 min. **g**,**-i**, Same as in panels **d**-**f** after repeating the same procedure as before (i.e. 1 h to reach room temperature, exposure to 4.8 L hydrogen, post-annealing at about 600 K). Measurement parameters: *U* = +1.0 V for panels **a**,**b**,**d**,**e**,**g**,**h** and *U* = -0.2 V for panels **c**,**f**,**i**; *I* = 1 nA; *T* = 4-5 K; Cr bulk tip; scale bars 100 nm for panels **a**,**b**,**d**,**e**,**g**,**h**; scale bars 10 nm for panels **c**,**f**,**i**.

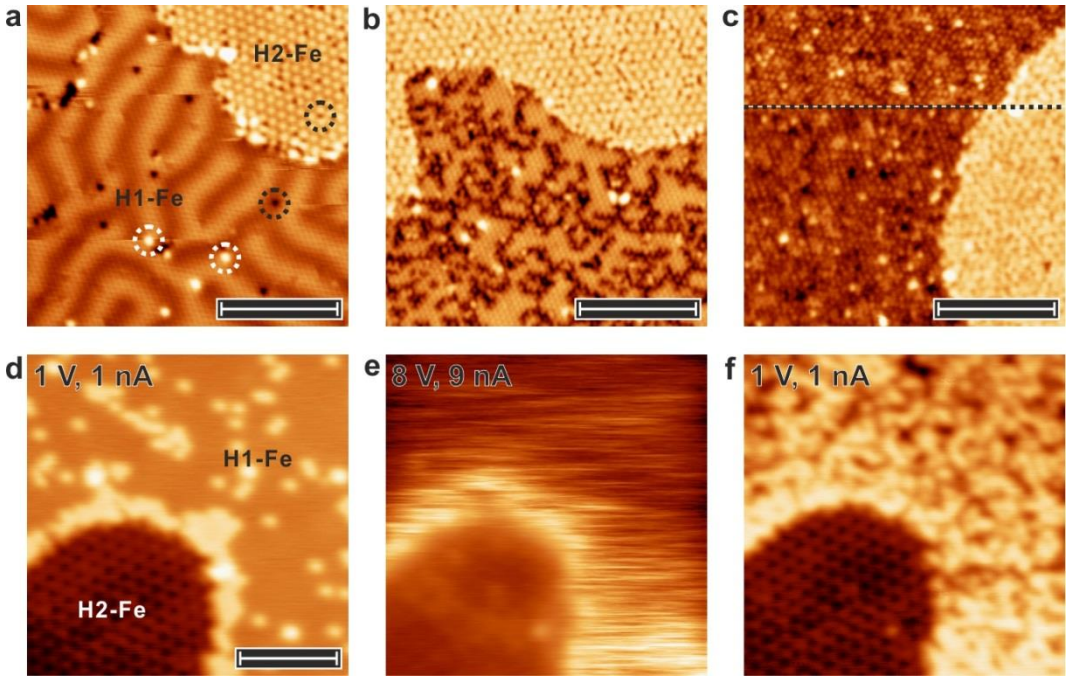

Supplementary Figure 2 | Disordered H-Fe phases and tip-induced disorder. a-c, Constant-current images of a measurement series with repeated exposure of Fe/Ir(111) to H at room temperature and subsequent annealing at about 600 K for 10 min: **a**, after exposure to 4.8 L of H; bright protrusions (hydrogen vacancies) and dark pits (extra hydrogen atoms) are highlighted by white and black dashed circles, respectively. **b**, after additional 4.8 L of H; **c**, after additional 48 L of H. The black dashed line indicates a tip change during scanning. Regardless of the degree of disorder within the superstructures, the boundary between the H1-Fe and H2-Fe areas remains abrupt. **d-f**, Constant-current images of a measurement series with changing tunnel parameters as indicated in the panels; comparison between panels **d** and **f** demonstrates a change of the H1-Fe phase due to the extreme tunneling conditions in panel **e**. Measurement parameters for panels **a**-**c**: U = -0.5 V; I = 1 nA; all: T = 4-5 K; Cr bulk tip; scale bars 10 nm for panels **a-c**; scale bar 6 nm for panel **d**.

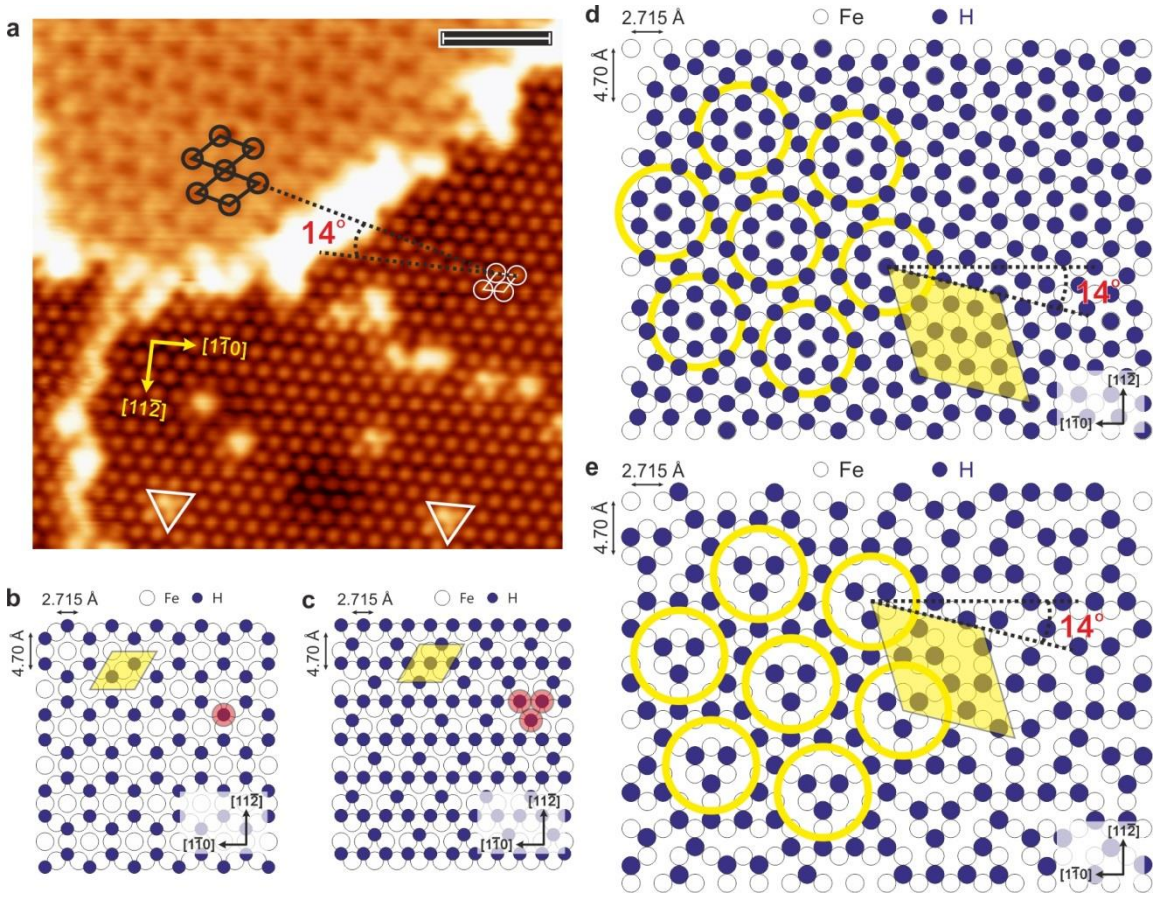

Supplementary Figure 3 | Possible structural models of the H-induced superstructures displayed for a single hexagonal Fe layer. a, High resolution STM constant-current topography image of H1-Fe and H2-Fe. The angle between the close-packed directions of the hexagonal lattices observable for the superstructures is 14°. The hydrogen vacancies (bright protrusions) with the same geometrical shape have been marked by white triangles. Scale bar 3 nm. **b**,**c**, Possible H1-Fe superstructure models for 0.50 ML and 0.75 ML H coverages, respectively. Yellow diamonds denote the unit cell of the superstructure, which is aligned along the high-symmetry lines of the Ir (111) surface due to the p(2×2) structure. The solid red circles indicate possible missing H atoms for the hydrogen vacancies shown in panel **a**. **d**,**e**, Possible H2-Fe superstructure models with 16 and 9 H atoms in a unit cell of 13 Fe atoms. Yellow diamonds denote the unit cells of the H2-Fe structure, while yellow circles illustrate the hexagonal lattice of the superstructure.

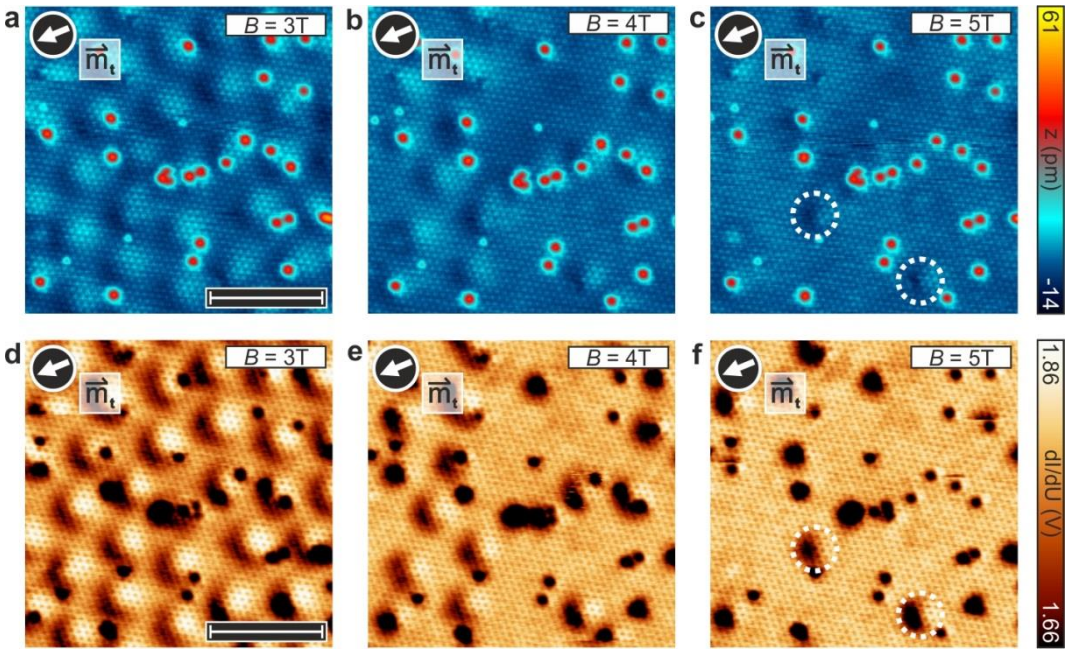

Supplementary Figure 4 | Identification of skyrmions and defects. a,**-c**, Spin-polarized constant-current images of the same sample area at different applied magnetic fields as indicated in the panels. Defects appear as protrusions and magnetic skyrmions can be identified by their two-lobe structure (brighter to the top right and darker to the bottom left). The number of skyrmions decreases as the magnetic field is increased, see white dashed circles in panel **c** for some skyrmions remaining at 5 T. **d**,**-f**, Maps of differential tunneling conductance acquired simultaneously with the constant-current images; at this bias voltage the defects appear dark, whereas the magnetic skyrmions have a very similar appearance compared to the constant-current images. Measurement parameters: U = -0.2 V; I = 1.0 nA; T = 4.2 K; Cr bulk tip; scale bars 8 nm.

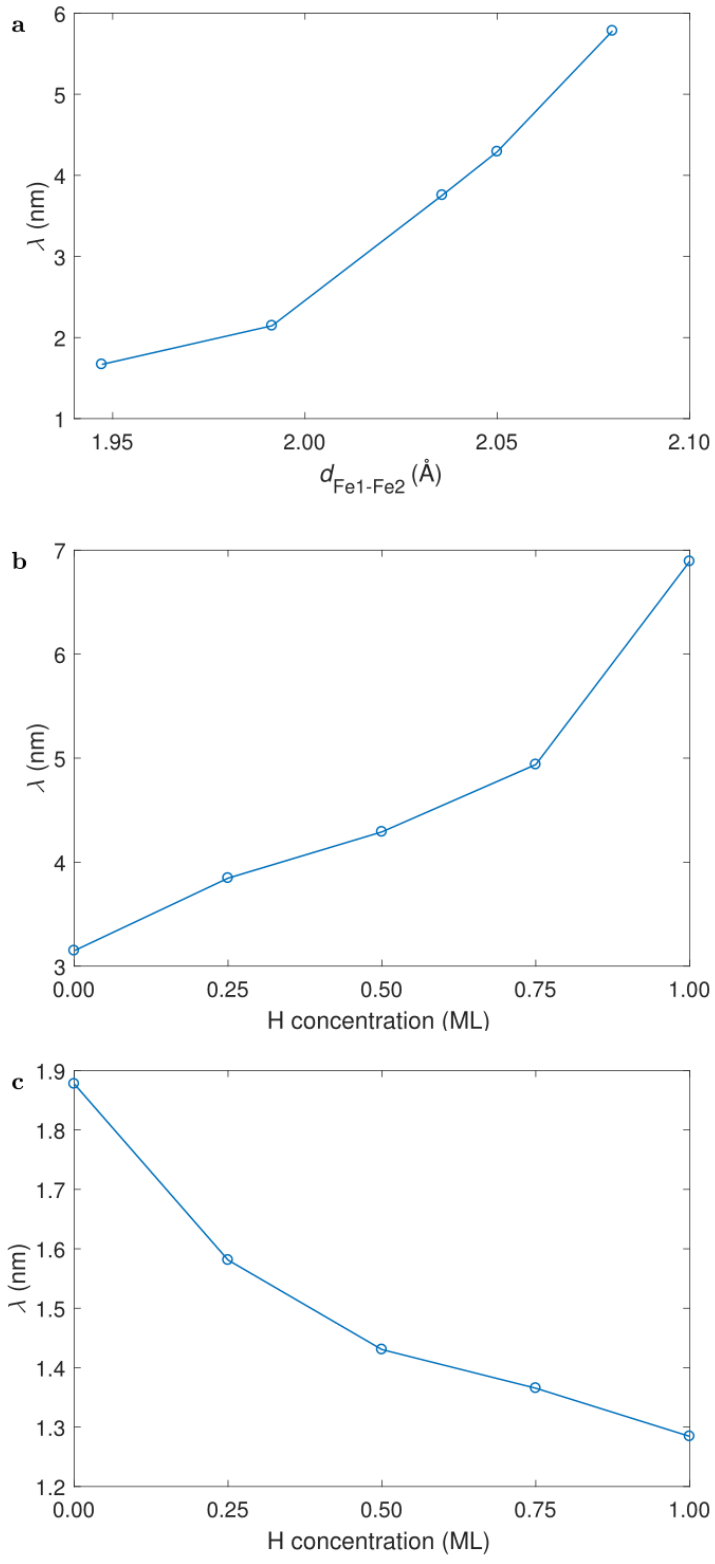

Supplementary Figure 5 | Dependence of the spin spiral period on calculation parameters. a, Dependence of the period on the Fe1-Fe2 interlayer distance, with the other layer distances and H concentration kept fixed at the value for the system modelling the H1-Fe structure (0.50 ML H coverage in Fe1-Fe2 A position). **b**, Dependence of the spin spiral period on the H concentration, with the other parameters again kept fixed at the values for the H1-Fe model. **c,** Dependence of the spin spiral period on the H concentration, with the fixed geometry of the H in the Fe2-Vac A position.

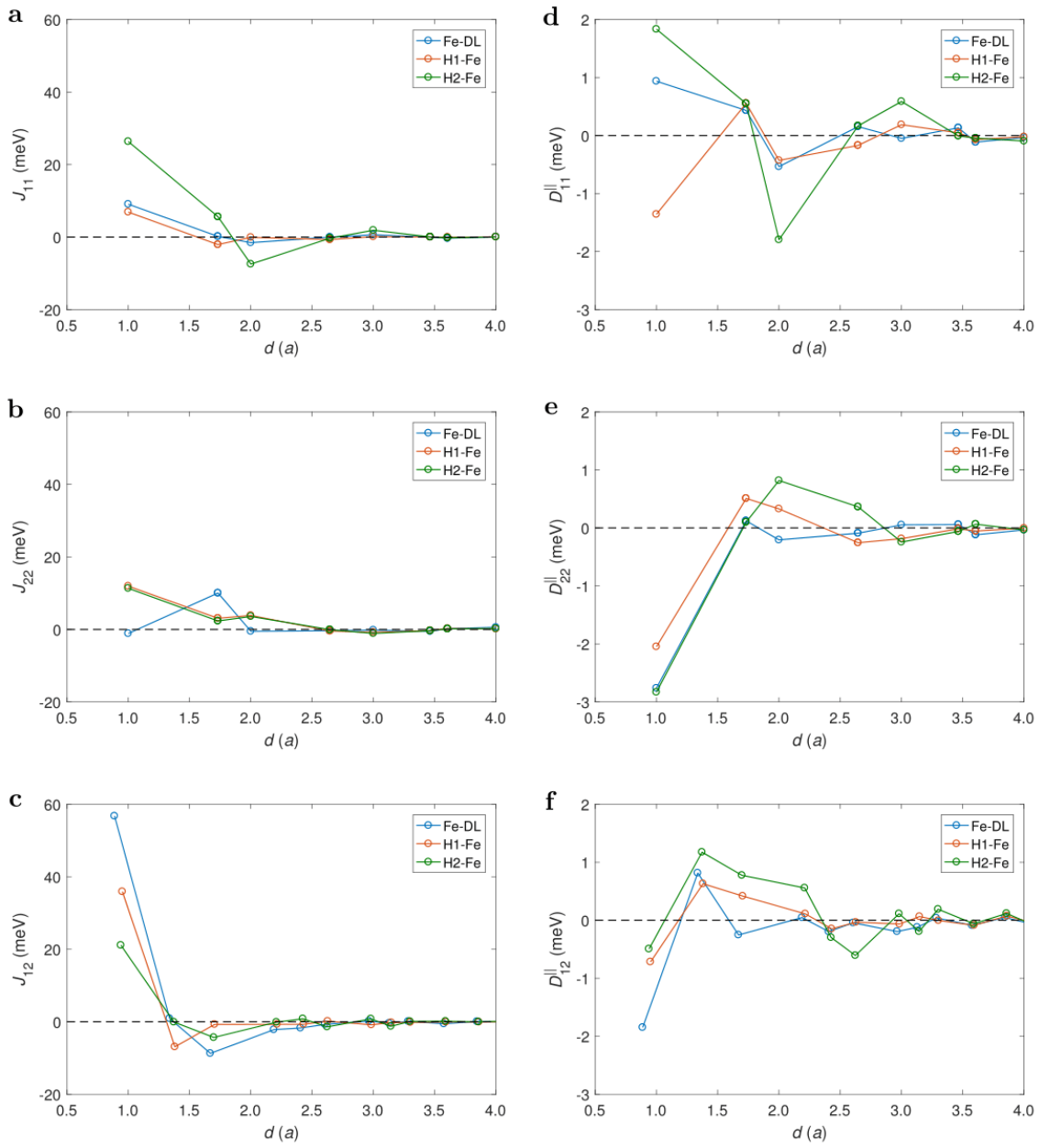

Supplementary Figure 6 | Spin interaction parameters calculated from the relativistic torque method with the SKKR program. a,**-c**, Heisenberg exchange interactions within **a**, the first and **b**, the second Fe layers, as well as **c**, between the two Fe layers as a function of distance between the neighbours. The values are given for the Fe-DL, H1-Fe (0.50 ML H at Fe1-Fe2 A) and H2-Fe (H at Ir-Fe1 C) systems investigated in the main text. Positive and negative values denote ferromagnetic and antiferromagnetic couplings, respectively. **d**,**-f**, In-plane component of the Dzyaloshinsky–Moriya vectors. Positive and negative values prefer left- and right-handed rotations, respectively.

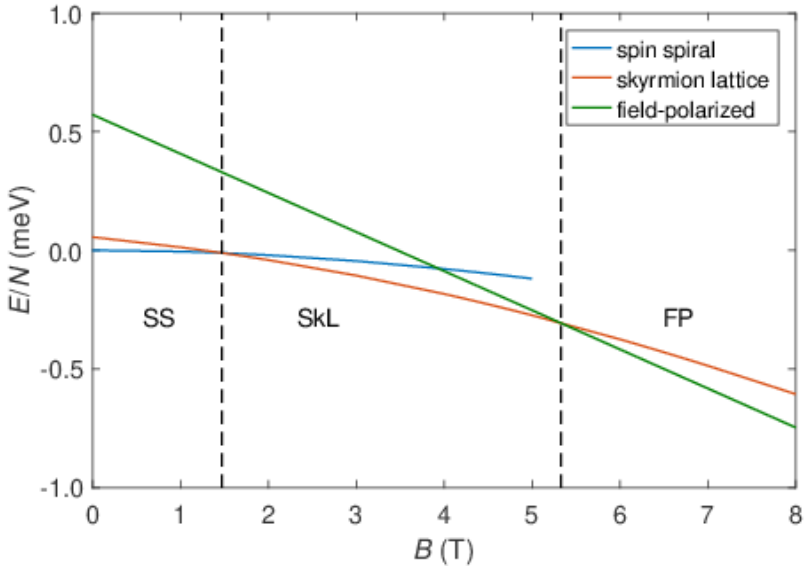

Supplementary Figure 7 | Zero-temperature phase diagram calculated from the *ab initio* interaction parameters. The interaction parameters are displayed in Supplementary Fig. 6 for the H1-Fe system. The phase diagram shows reasonable quantitative agreement with the one determined using the simplified model parameters, Fig. 5 in the main text.

Ir/Fe1/Fe2	E (eV)	Fe1 μ (μ_B)	Fe2 μ (μ_B)	Ir-Fe1 d (Å)	Fe1-Fe2 d (Å)
A/B/C	0.000	2.45	2.70	2.09	1.82
A/B/A	0.070	2.31	2.67	2.10	1.78
A/C/B	0.017	2.50	2.71	2.09	1.84
A/C/A	0.096	2.35	2.67	2.10	1.80

Supplementary Table 1 | Results of VASP calculations for different stackings of the Fe double layer. The table displays energies E, magnetic moments μ and interlayer distances d. The energies are given with respect to the lowest energy A/B/C stacking.

H position	E (eV)	Fe1 μ (μ_B)	Fe2 μ (μ_B)	Ir-Fe1 d (Å)	Fe1-Fe2 d (Å)	H Q (e)
Fe2-Vac A	0.000	2.45	2.27	2.09	1.90	1.22
Fe2-Vac B	0.033	2.50	2.27	2.09	1.89	1.22
Fe2-Vac C	1.127	2.42	2.36	2.06	2.01	0.96
Fe1-Fe2 A	0.616	2.33	2.38	2.08	2.11	1.36
Fe1-Fe2 B	0.671	2.49	2.16	2.06	2.10	1.36
Fe1-Fe2 C	0.848	2.15	2.79	2.12	2.15	1.38
Ir-Fe1 A	1.055	2.29	2.76	2.50	1.85	1.24
Ir-Fe1 B	1.652	2.52	2.65	2.68	1.74	0.92
Ir-Fe1 C	1.158	2.07	2.83	2.27	2.01	1.21

Supplementary Table 2 | Results of VASP calculations for different H adsorption sites on the Fe double layer. The stacking for the Fe-DL was A/B/C. The table displays energies E, magnetic moments μ, interlayer distances d and Bader charges Q. The energies are given with respect to the lowest energy Fe2-Vac A adsorption site.

H coverage	Fe1 μ (μ_B)	Fe2 μ (μ_B)	Ir-Fe1 d (Å)	Fe1-Fe2 d (Å)	H Q (e)
0.00 ML	2.45	2.70	2.09	1.82	0.00
0.25 ML	2.45	2.69	2.08	1.96	1.39
0.50 ML	2.40	2.62	2.07	2.05	1.38
0.75 ML	2.36	2.50	2.07	2.09	1.37
1.00 ML	2.33	2.38	2.08	2.11	1.36

Supplementary Table 3 | Results of VASP calculations for different H concentrations on the Fe double layer. The Fe1-Fe2 A (octahedral between the layers) adsorption site was considered for H. The 0.00 ML coverage corresponds to the A/B/C stacking of the Fe layers in the pristine Fe-DL from Supplementary Table 1. The 1.00 ML coverage corresponds to the Fe1-Fe2 A position from Supplementary Table 2. The table displays magnetic moments μ, interlayer distances d and Bader charges Q. The magnetic moments and the vertical positions were averaged over Ir, Fe and H atoms belonging to the same atomic layer in the p(2×2) unit cell.

H position	Fe1 μ_S (μ_B)	Fe2 μ_S (μ_B)	H Q (e)
Fe-DL	2.87	2.92	0.00
Fe2-Vac A	2.50	2.93	1.22
Fe1-Fe2 A	2.71	2.66	1.36
Ir-Fe1 C	2.37	2.77	1.19
H coverage	Fe1 μ_S (μ_B)	Fe2 μ_S (μ_B)	H Q (e)
0.00 ML	2.87	2.92	0.00
0.25 ML	2.90	2.96	1.44
0.50 ML	2.83	2.86	1.41
0.75 ML	2.76	2.76	1.38
1.00 ML	2.71	2.66	1.36

Supplementary Table 4 | Results of SKKR calculations for different H adsorption sites and concentrations. The table displays spin magnetic moments μ_s and charges Q, compare Supplementary Tables 2-3 for the VASP data. The 0.00 ML and 1.00 ML coverages correspond to the Fe-DL and Fe1-Fe2 A rows in the H position table, respectively.

system	$\mathcal{J}_1$ (10^{-12}J m^{-1})	$\mathcal{J}_2$ (10^{-30}J m)	$\mathcal{D}$ (10^{-3}J m^{-2})	$\mathcal{K}$ (10^{6}J m^{-3})
Fe-DL	-12.69	0.39	-6.99	3.16
H1-Fe	0.00	0.35	-6.05	-0.13
H2-Fe	4.35	0.37	-1.46	3.34

Supplementary Table 5 | Micromagnetic parameters for the model systems. Negative values of $\mathcal{J}_1$ indicate a spin spiral state formed by the frustrated Heisenberg exchange interactions, cf. $f = (J_1 + 3J_2)/J_1$ in Table 1 of the main text with the atomistic parameters. Negative sign of $\mathcal{D}$ prefers a right-handed rotation of the spins. Positive and negative signs of $\mathcal{K}$ denote easy-axis and easy-plane anisotropies, respectively.

Supplementary Note 1 | The different hydrogen-induced phases H1-Fe and H2-Fe.

The growth of Fe on Ir(111) changes with layer thickness. Whereas the first monolayer grows pseudomorphically with respect to the substrate[1], the second monolayer releases strain by the incorporation of dislocation lines along the $[11\overline{2}]$ directions[2]. Supplementary Figures 1a and 1b show a constant-current image and a simultaneously acquired d*I*/d*U* map, respectively, of a sample of about 2.2 atomic layers of Fe on Ir(111). On the Fe double layer (Fe-DL) the dislocation lines form arrays with distances of about 5 nm. Some pseudomorphic Fe-DL regions exist between these arrays. The magnified view presented in Supplementary Fig. 1c demonstrates that the magnetic spin spiral in the reconstructed Fe-DL is unchanged by external magnetic fields up to 9 T.

When atomic hydrogen is dosed onto this sample at room temperature (about 1 hour after removal from the 4.2 K STM) and the sample is annealed afterwards, the morphology changes, see Supplementary Figs. 1d-f: the number of dislocation lines is strongly reduced[3], most of the Fe-DL area exhibits a p(2×2) superstructure (H1-Fe) with several defects, and some islands with a 0.98 nm periodic superstructure (H2-Fe) are formed. A similar disappearance of reconstructed areas on the Ir(100) surface upon hydrogen adsorption has been demonstrated earlier[4], attributed to the saturation of the truncated bonds of surface atoms by the adsorbant. Upon additional exposure of the same sample to hydrogen at room temperature and subsequent annealing, the sample changes again, as seen in Supplementary Figs. 1g-i: the H1-Fe phase is now well-ordered, i.e. the amount of hydrogen is now sufficient to form the p(2×2) superstructure. The H2-Fe islands are now larger, but the ratio of the two areas has not changed. We conclude that the two phases cannot easily be transformed into each other. However, since the H2-Fe islands can coalesce during annealing, this also leads to well-defined and more extended areas of the H1-Fe structure where skyrmions can form under the application of an external field. Such a sample was used for the investigations shown in Fig. 2 of the main text.

Based on our measurements we can derive neither the H concentration nor the vertical or lateral adsorption sites of the H atoms. However, we find that there is always a sharp boundary between the two H-Fe superstructures, even if one or both of the phases are rather disordered due to insufficient or excessive H exposure or treatment at very high temperature, see Supplementary Figs. 2a-c. If the two phases would differ in their H concentration only, a more gradual transition between the two would be expected, in particular when a phase is already disordered. Thus we suspect that the two H-Fe superstructures originate from different vertical positions of the H atoms with respect to the surface.

The repeated dosages of hydrogen also shed light on the origin of two types of point defects, namely bright protrusions and dark pits in constant-current topography images. By comparing Supplementary Figs. 1f and 1i, it can be observed that the number of bright protrusions on top of the H1-Fe and at the edge of the H2-Fe drops significantly after exposure to an additional amount of 4.8 L hydrogen, which allows us to identify the nature of these protrusions as hydrogen vacancies. Once the H1-Fe and the H2-Fe have incorporated a sufficient amount of atomic hydrogen, further hydrogen exposure will turn them into disordered phases and the additional hydrogen atoms on top of them appear as dark pits as shown in Supplementary Figs. 2a and b. In Supplementary Fig. 2a, the hydrogen vacancies (bright protrusions) and extra hydrogen atoms (dark pits) have been indicated by white and black dashed circles, respectively.

The different impact of measurements at high bias voltage on the two phases also suggests different adsorption sites, see measurement series in Supplementary Figs. 2d-f: First, a sample area with both H1-Fe and H2-Fe is imaged with tunneling parameters of U = 1.0 V and I = 1 nA, see panel d. Next, the same area is scanned with a high voltage of U = 8.0 V and a high current of I = 9 nA, see panel e. Finally, with the same imaging parameters as used in panel d, it becomes evident that these extreme tunneling parameters strongly affected the H1-Fe phase, where a tip-induced disorder is observed, whereas the H2-Fe is hardly altered, compare panels d and f. This suggests that the hydrogen in the H2-Fe phase is bound much stronger, possibly closer to the Ir-Fe interface than in the H1-Fe phase.

The observed superstructures allow for several different structural models with different H concentrations, several of which are visualized in Supplementary Fig. 3. The p(2×2) H1-Fe could be realized by H atoms in both fcc and hcp hollow sites with a H:Fe ratio of 1:2, as seen in the simplified ball model with a single atomic Fe layer in Supplementary Fig. 3b. An alternative is the adsorption of H in 3 out of 4 hollow sites of the same type, see Supplementary Fig. 3c, resulting in a H concentration of 0.75 with respect to one Fe atom in the unit cell. Since hydrogen vacancies (bright protrusions) on top of the H1-Fe exhibit the same geometrical shape, indicated by white triangles pointing along the $[11\bar{2}]$ direction in Supplementary Fig. 3a, we are able to infer the positions from which the H atoms are possibly missing in the structural models, marked by solid red circles in Supplementary Figs. 3b and c. The 0.98 nm period H2-Fe supercell comprises 13 Fe atoms, and it is rotated with respect to the high-symmetry lines of the Ir (111) surface by about ±14°, forming two rotational domains as can be seen, e.g., for the two islands in Fig. 2 of the main text. Several different H-loaded states can be constructed for this supercell, two of which are shown in Supplementary Figs. 3d and 3e with 16 and 9 H atoms per unit cell in different adsorption sites in this single-layer model.

Supplementary Note 2 | Identification of skyrmions and defects.

To distinguish structural and magnetic features in STM, it is useful to compare topographic constant-current images and simultaneously acquired differential tunneling conductance (dI/dU) maps. For the measurement shown in Fig. 3 of the main text, this data is displayed in Supplementary Fig. 4. In the topography image the defects due to incomplete formation of the H1-Fe phase are imaged as bright protrusions, whereas in the dI/dU maps they appear as darker dots. In contrast, in this measurement with a magnetic tip being dominantly sensitive to the in-plane sample magnetization component, the magnetic contribution to the signals appears similar in both measurement channels.

Supplementary Note 3 | VASP calculations.

For the pristine Fe-DL, different stacking orders of the layers were compared as shown in Supplementary Table 1. Ideally the fcc Ir lattice grows in A/B/C stacking along the (111) direction, with an interlayer distance of $\sqrt{2/3}a = 2.21$ Å. The distance between the top Ir layer and the one below it was slightly larger than this value (2.28 Å) and only very weakly depended on the considered H adsorption sites and concentrations. On the other hand, the Ir-Fe1 and Fe1-Fe2 distances were reduced by approximately 10 pm and 40 pm compared to the ideal interlayer distance due to the smaller bulk lattice constant of Fe, which is also responsible for the appearance of reconstruction lines in the experiments. We only took into account stackings preserving the C_{3v} symmetry of the system, since the hydrogenated structures also displayed this symmetry due to the disappearance of reconstruction lines. Reconstructed geometries in the same system have been investigated recently in ref. 5. We found that the stacking continuing the A/B/C order has the lowest energy, and the non-

collinear magnetic structure was only investigated for this stacking with the SKKR code, where the obtained spin spiral period was found to be in reasonable agreement with the experiments. Therefore, in the following calculations only this stacking was considered, although we cannot exclude that the H adsorption also changes the stacking of the Fe layers.

For a full monolayer of H coverage, we considered nine possible adsorption sites as summarized in Supplementary Table 2, all of them preserving the C_{3v} symmetry, which was also observed in the experiments. The lowest energy corresponds to the fcc adsorption site on the surface (Fe2-Vac A). In this case, the top Fe2 layer moves slightly away from the substrate (by about 8 pm), similarly to the H adsorption effect on Fe/Ir(001) investigated in ref. 6. However, the SKKR calculations demonstrated that this adsorption site actually leads to a decrease in the magnetic period, contrary to the experimental findings. Furthermore, the experimental observations discussed in Supplementary Note 1 indicated that the H1-Fe and H2-Fe structures may be due to the adsorption of H at different distances from the surface. Therefore, we also determined the magnetic interactions between the Fe atoms for H in the octahedral position between the Fe layers (Fe1-Fe2 A) and at the Ir-Fe interface (Ir-Fe1 C). Although these states have significantly higher energies, in earlier calculations performed for the surface of bulk bcc Fe it was found[7] that the H atoms may overcome energy differences of similar magnitude when diffusing into the metal. The distance between the Fe layers in these configurations was increased by about 30 and 20 pm with respect to the pristine Fe-DL, leading to a significant enhancement of the magnetic period. Furthermore, for H between the substrate and the magnetic layers the Ir-Fe distance also increased by about 20 pm, which was found to be responsible for the weakening of the Dzyaloshinsky–Moriya interaction and the formation of the ferromagnetic ground state as discussed in the main text.

Supplementary Table 2 also displays the Bader charges[8,9,10] for H, indicating that in most considered adsorption sites charge is transferred from the Fe to the H atoms[7,11]. This charge transfer is maximal for H between the magnetic layers with 4 or 6 Fe neighbours and lower for H at the Ir-Fe and Fe-Vac interfaces with only 3 Fe neighbours. Finally, the obtained Bader charge of H is below 1 if it has only a single Fe neighbour (Fe2-Vac C, Ir-Fe1 B), which can be explained by the H orbitals extending into the vacuum or an opposite direction of charge transfer between H and Ir. The charge transfer is accompanied by a decrease of the Fe magnetic moments, especially in the layers directly neighbouring the H atom.

Finally, we also investigated the effect of different H coverages to obtain a more accurate description of the H1-Fe structure, which was found to exhibit a $\mathrm{p}(2\times2)$ atomic superstructure in the experiments. The results are summarized in Supplementary Table 3, with the parameters averaged over atoms nominally belonging to the same atomic layer. We assumed that the H is adsorbed into the octahedral positions between the two Fe layers (Fe1-Fe2 A), since earlier it was found that this leads to a significant increase of the magnetic period. We considered 1, 2 or 3 H atoms in these sites in the $\mathrm{p}(2\times2)$ unit cell. As expected, both the increase in the Fe1-Fe2 interlayer distance and the decrease in the magnetic moments is monotonic in the H coverage, which also leads to a monotonic increase in the spin spiral period as shown in Fig. 4b in the main text.

Supplementary Note 4 | SKKR self-consistent calculations.

For comparison with the VASP calculations, the spin magnetic moments determined in the ferromagnetic configuration and the charges on the H atoms from the SKKR calculations are summarized in Supplementary Table 4. As mentioned in the Methods section, the Wigner–Seitz radii of the atomic spheres were determined in such a way as to minimize the overlap between the spheres. In the case of the H atoms, this meant that the charge inside the sphere must approximate the Bader charge determined from VASP calculations, otherwise it would be possible that the atomic sphere cuts deeply inside the electron cloud of the neighbouring Fe atoms. With such a choice of the Wigner–Seitz radii, it is clear that the SKKR calculations reproduce the decrease in the magnetic moments due to H adsorption observed in the VASP calculations. A slight deviation from this trend can be observed between 0.00 ML and 0.25 ML concentrations for the magnetic moments, but this can be explained by the fact that no H atomic sphere was included in the calculations for the Fe-DL at 0.00 ML coverage.

Supplementary Note 5 | Dependence of the spin spiral period on *ab initio* calculation parameters.

During the *ab initio* calculations it is possible to tune all calculation parameters independently of each other, enabling one to separate the contribution of different effects on the spin spiral period. As shown in Supplementary Fig. 5, we performed investigations for the model describing the H1-Fe system (0.50 ML H coverage in the Fe1-Fe2 A position) by changing the distance between the Fe layers and the H concentration. Supplementary Figure 5a displays that modifying the interlayer distance by about 15 pm enhances the magnetic period by about a factor of four. A similar correlation between the substrate-magnetic layer distance and the magnetic period has been pointed out in several earlier publications[1,12,13,14,15,16], generally in connection with the decreased hybridization as mentioned in the main manuscript. It is important to note that there is some uncertainty in the interlayer distances determined from *ab initio* calculations due to the different types of approximations involved. For example, we observed that using the Perdew-Burke-Ernzerhof[17] (PBE) parametrization of the exchange-correlation potential instead of the PW91[18] method mentioned in the Methods section changes the Fe1-Fe2 distance by about 2 pm in the VASP calculations. Switching to the local density approximation (LDA) from the generalized gradient approximation (GGA) is expected to have an even larger influence[12]. For a fixed interlayer distance, the magnetic period determined from the SKKR method also depends on the type of exchange-correlation potential. However, the predictions that the inclusion of H between the Fe layers or at the Ir-Fe interface increases the interlayer distance, and the enhancement of this distance leads to a larger magnetic period, are independent of the exact forms of approximations involved in the calculations; therefore, they may be used for a comparison with the experimental observations.

Tuning the H concentration in a fixed geometry may have various effects on the calculated magnetic period depending on the adsorption sites, as shown in Supplementary Figs. 5b,c. For the H between the Fe atomic layers (see Supplementary Fig. 5b), an increase of the magnetic period by about a factor of two is obtained between 0.00 ML and 1.00 ML of H. This indicates that in this geometry the hybridization between Fe and H atomic orbitals has an analogous effect to the increase of the Fe interlayer distance. In contrast, Supplementary Fig. 5c shows the concentration dependence if H is adsorbed on top of the Fe layers in the fcc (Fe2-Vac A) positions. At 0.00 ML concentration the spin spiral period is somewhat larger than for the Fe-DL due to the slightly increased Fe1-Fe2 distance – see Supplementary Table 2 –, around 1.9 nm compared to 1.4 nm. On the other hand, the H-Fe

hybridization counteracts this effect in this case and leads to a reduction in the spin spiral period as the H concentration is increased, also displayed in Fig. 4a of the main text, with a 1.3 nm period for 1.00 ML coverage in this adsorption position.

Supplementary Note 6 | Connection between *ab initio* interaction parameters, the simplified model and the micromagnetic description.

As mentioned in the Methods section, the interaction coefficients between the spins were determined from the relativistic torque method[19] for all neighbours within a radius of $8a$. The classical spin Hamiltonian describing the system reads

$$H = -\frac{1}{2}\sum_{i\neq j}\mathbf{S}_i\mathbf{J}_{ij}\mathbf{S}_j - \sum_i \mathbf{S}_i\mathbf{K}_i\mathbf{S}_i - \sum_i \mu_{\mathrm{s},i}\mathbf{S}_i\mathbf{B}, \qquad (1)$$

with $\mathbf{S}_i$ unit vectors representing the spins at site i, $\mu_{\mathrm{s},i}$ layer-dependent spin magnetic moments and $\mathbf{B}$ the external magnetic field. The $\mathbf{K}_i$ layer-dependent on-site anisotropy tensor may be characterized by a single value K_i^{zz} in the considered symmetry class. From the $\mathbf{J}_{ij}$ interaction tensor it is possible to determine the Heisenberg exchange interactions $J_{ij} = \frac{1}{3}J_{ij}^{\alpha\alpha}$ and the Dzyaloshinsky–Moriya vectors $D_{ij}^{\alpha} = \frac{1}{2}\varepsilon^{\alpha\beta\gamma}J_{ij}^{\beta\gamma}$; summation over Cartesian indices α, β, γ appearing twice is understood in the expressions. For the Fe-DL, H1-Fe and H2-Fe structures discussed in the main text, these parameters are displayed in Supplementary Fig. 6. Both the Heisenberg and the Dzyaloshinsky–Moriya exchange coefficients display an oscillatory decay, typical for RKKY-like interactions[20,21,22] in ultrathin magnetic systems on heavy metal substrates[23]. The difference between the diagonal components of the interaction tensor also contributes to the total magnetic anisotropy energy as $E_{\mathrm{ani},i} = \frac{1}{2}\sum_j\left(J_{ij}^{zz} - J_{ij}^{xx}\right) + K_i^{zz}$.

Considering interaction parameters with many different neighbours is essential in correctly describing the high-energy behaviour of the system[14], for example, in simulations performed at higher temperatures[24]. It was demonstrated recently that if the interaction parameters determine different magnetic periods in the different atomic layers, this can lead to a significant modulation of the spin spiral wavelength as the temperature is increased[25]. However, the investigations for the present system were carried out at low temperature and the shape of the equilibrium spin structures was considered, and it is expected that the simplified model given in Eq. (1) and Fig. 5 of the main text can correctly account for these effects. As demonstrated in Supplementary Fig. 7, we indeed obtained a very similar zero-temperature phase diagram for the H1-Fe system to Fig. 5 if the calculations were carried out with the *ab initio* interaction parameters instead of the simplified model, similarly to the observation in ref. 26.

The simplified model parameters in Eq. (1) were determined as follows. The energy of the spin spirals was calculated for harmonic configurations in the plane defined by the surface normal vector $\mathbf{n}$ and an in-plane unit vector $\mathbf{e}$,

$$\mathbf{S}_i = \mathbf{n}\cos\mathbf{k}\mathbf{R}_i + \mathbf{e}\sin\mathbf{k}\mathbf{R}_i, \qquad (2)$$

which transforms into Eq. (2) in the Methods section for cycloidal spin spirals where $\mathbf{e}$ is along the wave vector direction. For a fixed direction of $\mathbf{e}$ replacing $\mathbf{k}$ by $-\mathbf{k}$ switches the chirality of the spiral. The energy per spin reads[27]

$$\frac{1}{N}E_{\mathrm{SS}}(\mathbf{k}) = \frac{1}{n_{\mathrm{layer}}}\sum_{\mathrm{layers}}\left(E_{\mathrm{symm},i} + E_{\mathrm{antisymm},i} + E_{\mathrm{ani},i}\right), \tag{3}$$

$$E_{\mathrm{symm},i} = -\frac{1}{2}\sum_{\mathbf{R}_j-\mathbf{R}_i}\frac{1}{2}\left(\mathbf{e}\mathbf{J}_{ij}\mathbf{e} + \mathbf{n}\mathbf{J}_{ij}\mathbf{n}\right)\cos\left[\mathbf{k}\left(\mathbf{R}_j - \mathbf{R}_i\right)\right], \tag{4}$$

$$E_{\mathrm{antisymm},i} = -\frac{1}{2}\sum_{\mathbf{R}_j-\mathbf{R}_i}\mathbf{D}_{ij}(\mathbf{e}\times\mathbf{n})\sin\left[\mathbf{k}\left(\mathbf{R}_j - \mathbf{R}_i\right)\right], \tag{5}$$

$$E_{\mathrm{ani},i} = -\frac{1}{2}(\mathbf{e}\mathbf{K}_i\mathbf{e} + \mathbf{n}\mathbf{K}_i\mathbf{n}), \tag{6}$$

which has to be compared to that of the ferromagnetic state,

$$\frac{1}{N}E_{\mathrm{FM}} = \frac{1}{n_{\mathrm{layer}}}\sum_{\mathrm{layers}}\left(-\frac{1}{2}\sum_{\mathbf{R}_j-\mathbf{R}_i}\mathbf{n}\mathbf{J}_{ij}\mathbf{n} - \mathbf{n}\mathbf{K}_i\mathbf{n}\right). \tag{7}$$

The dispersion relations were calculated for 128×128 $\mathbf{k}$ points in the Brillouin zone for the Fe-DL and 512×512 $\mathbf{k}$ points for the hydrogenated structures. The energy difference between the spin spiral at zero wave vector and the energy of the ferromagnetic state is half of $E_{\mathrm{ani},i}$ averaged over the layers, which was identified with half of the anisotropy parameter K in Eq. (1).

If the spin spiral dispersion relations are calculated from the model given by Eq. (1), the symmetric and antisymmetric contributions read

$$E_{\mathrm{symm}} = -J_1\left[\cos(k^x a) + 2\cos\left(\frac{1}{2}k^x a\right)\cos\left(\frac{\sqrt{3}}{2}k^y a\right) - 3\right]$$

$$-J_2\left[\cos\left(\sqrt{3}k^y a\right) + 2\cos\left(\frac{3}{2}k^x a\right)\cos\left(\frac{\sqrt{3}}{2}k^y a\right) - 3\right], \tag{8}$$

$$E_{\mathrm{antisymm},xz} = -D\left[\sin(k^x a) + \sin\left(\frac{1}{2}k^x a\right)\cos\left(\frac{\sqrt{3}}{2}k^y a\right)\right], \tag{9}$$

$$E_{\mathrm{antisymm},yz} = -\sqrt{3}D\cos\left(\frac{1}{2}k^x a\right)\sin\left(\frac{\sqrt{3}}{2}k^y a\right), \tag{10}$$

for spin spirals rotating in the xz and yz planes, respectively; z denotes the out-of-plane direction, x is along the nearest-neighbour $(1\bar{1}0)$ and y is along the next-nearest-neighbour $(11\bar{2})$ direction. Note that the symmetric energy contribution was shifted to be equal to zero at zero wave vector. The interaction parameters collected in Table 1 in the main text were determined by fitting the two-dimensional dispersion relations with Supplementary Eqs. (8)-(10) in a range around the center of the Brillouin zone including the spin spiral energy minima. The model does not approximate the spin spiral dispersion relation well at higher wave vectors; therefore, it is not expected to correctly account for the high-temperature behaviour as discussed above.

The simplified atomic model essentially corresponds to a micromagnetic description formulated on a hexagonal lattice, which is also expected to be only applicable at low wave vectors and (unless the temperature dependence of the parameters is considered) at zero temperature. The micromagnetic model is defined by the free-energy density[28,29]

$$f_0 = \mathcal{J}_1(\boldsymbol{\nabla}\mathbf{S})^2 + \mathcal{J}_2(\boldsymbol{\nabla}^2\mathbf{S})^2 + \mathcal{D}w_D(\mathbf{S}) - \mathcal{K}(S^z)^2 - M\mathbf{BS}, \tag{11}$$

with $\mathbf{S}$ the unit length vector field, M the magnetization, $\mathcal{J}_1$ the exchange stiffness, $\mathcal{J}_2$ the higher-order exchange parameter, $\mathcal{D}$ the Dzyaloshinsky–Moriya interaction and $\mathcal{K}$ the anisotropy constant. The energy density of the Dzyaloshinsky–Moriya interaction reads

$$w_D(\boldsymbol{S}) = S^z\partial_x S^x - S^x\partial_x S^z + S^z\partial_y S^y - S^y\partial_y S^z, \tag{12}$$

with the sign convention that $\mathcal{D} > 0$ prefers left-handed rotation.

The connection between the simplified model parameters and the micromagnetic parameters may be obtained by expanding Supplementary Eqs. (8)-(10) at low wave vectors, yielding

$$E_{\text{symm}} = \frac{3}{4}a^2(J_1 + 3J_2)\mathbf{k}^2 - \frac{9}{192}a^4(J_1 + 9J_2)(\mathbf{k}^2)^2 + \mathcal{O}(k^6), \tag{13}$$

$$E_{\text{antisymm},xz} = -\frac{3}{2}aDk^x + \mathcal{O}(k^3), \tag{14}$$

$$E_{\text{antisymm},yz} = -\frac{3}{2}aDk^y + \mathcal{O}(k^3). \tag{15}$$

Comparing Supplementary Eq. (11) after spatial Fourier transformation to Supplementary Eqs. (13)-(15) leads to the correspondence

$$\mathcal{J}_1 = \frac{1}{V_{\text{WS}}}\frac{3}{4}a^2(J_1 + 3J_2), \tag{16}$$

$$\mathcal{J}_2 = -\frac{1}{V_{\text{WS}}}\frac{9}{192}a^4(J_1 + 9J_2), \tag{17}$$

$$\mathcal{D} = \frac{1}{V_{\text{WS}}}\frac{3}{2}aD, \tag{18}$$

$$\mathcal{K} = \frac{1}{V_{\text{WS}}}K, \tag{19}$$

$$M = \frac{1}{V_{\text{WS}}}\mu_{\text{s}}, \tag{20}$$

where V_{WS} denotes the volume occupied by a single Fe atom. This was determined from the Wigner–Seitz radii used for the SKKR calculations by averaging over the two magnetic layers, and can be well approximated by $V_{\text{WS}} \approx \frac{\sqrt{3}}{2}a^2t$, where the layer thickness t is the distance between the outer Fe2 and the top Ir layer divided by two.

The micromagnetic interaction coefficients are summarized in Supplementary Table 5 for the systems displayed in Table 1 of the main text. Supplementary Equation (16) explains the importance of the factor $f = (J_1 + 3J_2)/J_1$; for negative values one has $\mathcal{J}_1 < 0$, meaning that the micromagnetic model is only stabilized by the higher-order $\mathcal{J}_2$ term, and the Heisenberg exchange interactions already determine an energy minimum at finite wave vector $k = \sqrt{-\frac{\mathcal{J}_1}{2\mathcal{J}_2}}$.

Supplementary References

1. Heinze, S. et al. Spontaneous atomic-scale magnetic skyrmion lattice in two dimensions. *Nat. Phys.* **7**, 713-718 (2011).
2. Hsu, P.-J. et al. Guiding Spin Spirals by Local Uniaxial Strain Relief. *Phys. Rev. Lett.* **116**, 017201 (2016).
3. Reimer, P. M., Zabel, H., Flynn, C. P. & Dura, J. A. Extraordinary alignment of Nb films with sapphire and the effects of added hydrogen. *Phys. Rev.* B **45**, 11426-11429 (1992).
4. Arman, M. A. et al. Adsorption of hydrogen on stable and metastable Ir(100) surfaces. *Surf. Sci.* **656**, 66-76 (2017).
5. Hauptmann, N. et al. Revealing the correlation between real-space structure and chiral magnetic order at the atomic scale. Preprint at arXiv:1712.02717 (2017).
6. Máca, F., Kudrnovský, J., Drchal, V. & Redinger, J. Influence of oxygen and hydrogen adsorption on the magnetic structure of an ultrathin iron film on an Ir(001) surface. *Phys. Rev.* B **88**, 045423 (2013).
7. Jiang, D. E. & Carter, E. A. Diffusion of interstitial hydrogen into and through bcc Fe from first principles. *Phys. Rev.* B **70**, 064102 (2004).
8. Henkelman, G., Arnaldsson, A. & Jónsson, H. A fast and robust algorithm for Bader decomposition of charge density. *Comput. Mater. Sci.* **36**, 354-360 (2006).
9. Sanville, E., Kenny, S. D., Smith, R. & Henkelman, G. An improved grid-based algorithm for Bader charge allocation. *J. Comp. Chem.* **28**, 899-908 (2007).
10. Tang, W., Sanville, E. & Henkelman, G. A grid-based Bader analysis algorithm without lattice bias. *J. Phys.: Condens. Matter* **21**, 084204 (2009).
11. Bessarab, P. F., Uzdin, V. M. & Jónsson, H. Effect of hydrogen adsorption on the magnetic properties of a surface nanocluster of iron. *Phys. Rev.* B **88**, 214407 (2013).
12. Kudrnovský, J., Máca, F., Turek, I. & Redinger, J. Substrate-induced antiferromagnetism of a Fe monolayer on the Ir(001) surface. *Phys. Rev.* B **80**, 064405 (2009).
13. von Bergmann, K. et al. Observation of a Complex Nanoscale Magnetic Structure in a Hexagonal Fe Monolayer. *Phys. Rev. Lett.* **96**, 167203 (2006).
14. Dupé, B., Hoffmann, M., Paillard, C. & Heinze, S. Tailoring magnetic skyrmions in ultra-thin transition metal films. *Nat. Commun.* **5**, 4030 (2014).
15. Simon, E., Palotás, K., Rózsa, L., Udvardi, L. & Szunyogh, L. Formation of magnetic skyrmions with tunable properties in PdFe bilayer deposited on Ir(111). *Phys. Rev.* B **90**, 094410 (2014).
16. Rózsa, L., Udvardi, L., Szunyogh, L. & Szabó, I. A. Magnetic phase diagram of an Fe monolayer on W(110) and Ta(110) surfaces based on *ab initio* calculations. *Phys. Rev.* B **91**, 144424 (2015).
17. Perdew, J. P., Burke, K. & Ernzerhof, M. Generalized Gradient Approximation Made Simple. *Phys. Rev. Lett.* **77**, 3865-3868 (1997).
18. Perdew, J. P. & Wang, Y. Accurate and simple analytic representation of the electron-gas correlation energy. *Phys. Rev.* B **45**, 13244-13249 (1992).
19. Udvardi, L., Szunyogh, L., Palotás, K. & Weinberger, P. First-principles relativistic study of spin waves in thin magnetic films. *Phys. Rev.* B **68**, 104436 (2003).
20. Ruderman, M. A. & Kittel, C. Indirect Exchange Coupling of Nuclear Magnetic Moments by Conduction Electrons. *Phys. Rev.* **96**, 99-102 (1954).
21. Kasuya, T. A Theory of Metallic Ferro- and Antiferromagnetism on Zener's Model. *Prog. Theor. Phys.* **16**, 45-57 (1956).
22. Yosida, K. Magnetic Properties of Cu-Mn Alloys. *Phys. Rev.* **106**, 893-898 (1957).

23. Khajetoorians, A. A. et al. Tailoring the chiral magnetic interaction between two individual atoms. *Nat. Commun.* **7**, 10620 (2016).
24. Rózsa, L., Simon, E., Palotás, K., Udvardi, L. & Szunyogh, L. Complex magnetic phase diagram and skyrmion lifetime in an ultrathin film from atomistic simulations. *Phys. Rev.* B **93**, 024417 (2016).
25. Finco, A. et al. Temperature-Induced Increase of Spin Spiral Periods. *Phys. Rev. Lett.* **119**, 037202 (2017).
26. von Malottki, S., Dupé, B., Bessarab, P. F., Delin, A. & Heinze, S. Enhanced skyrmion stability due to exchange frustration. *Sci. Rep.* **7**, 12299 (2017).
27. Rózsa, L. et al. Skyrmions with Attractive Interactions in an Ultrathin Magnetic Film. *Phys. Rev. Lett.* **117**, 157205 (2016).
28. Michelson, A. Phase diagrams near the Lifshitz point. I. Uniaxial magnetization. *Phys. Rev.* B **16**, 577-584 (1977).
29. Rózsa, L. et al. Formation and stability of metastable skyrmionic spin structures with various topologies in an ultrathin film. *Phys. Rev.* B **95**, 094423 (2017).